Quasi-Conformal Transformation Optics as Applied to Linear Antenna Array Performance Enhancement

M. Salucci, G. Oliveri, N. Anselmi, G. Gottardi, and A. Massa

Abstract

This work presents an innovative Material-by-Design (*MbD*) technique aimed at improving the radiation features of existing linear active electronically-scanned arrays (*AESA*s). Such a performance enhancement (in terms of beam-width, directivity, and side-lobe level) is guaranteed without increasing the number of elements nor requiring the re-design of the radiators and/or feeding network. Thanks to a suitable customization and integration of the quasi-conformal transformation optics (*QCTO*) technique approach with a source inversion (*SI*) strategy, the developed methodology enables the synthesis of meta-material enhancing radomes with reduced complexity (in terms of anisotropy indexes) able to let the original array reproduce the radiation performance of larger *target* apertures. Some representative numerical results are shown in order to validate the effectiveness of the proposed *MbD* approach, by taking into account the existing trade-off between the achievable boost and the overall cost in terms of complexity of the *QCTO*-synthesized meta-materials.

1 Extensiove Analysis - Half-Cosine Profile - $h' = 4.0$ [λ], $l' = 0.0$ [λ], $t' = 16.0$ [λ], $N = 15$

1.1 Step 1: Expanding the physical array ($N = 15$, $L = 7.0$ [λ])

Input Parameters

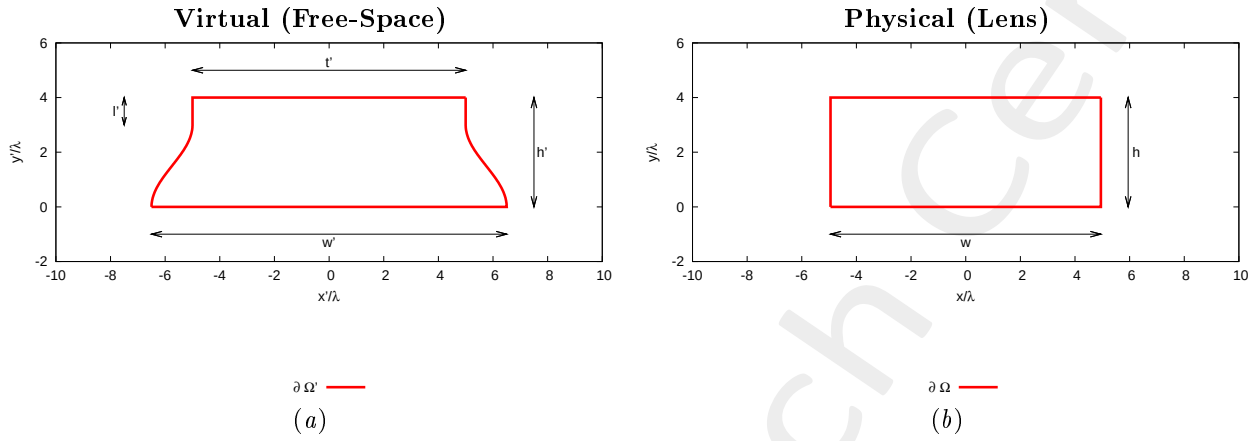

Figure 1: Transformation regions. The lower side of both virtual and physical boundaries are supposed to be PEC.

- **Virtual Geometry**

# Test Case	h' [λ]	l' [λ]	t' [λ]	w' [λ]
1	4.0	0.0	16.0	**17.8**
2	4.0	0.0	16.0	**19.0**
3	4.0	0.0	16.0	**19.8**
4	4.0	0.0	16.0	**20.7**
5	4.0	0.0	16.0	**21.4**

Table I: Considered virtual geometries. The values of w' have been empirically determined in order to achieve an aperture of the virtual array (L') equal to a multiple of $\lambda/2$. It is imposed that $h = h'$, while w is not controlled by the user.

- **Physical Array**
  - Number of elements, spacing, aperture: $N = 15$, $d = \frac{\lambda}{2}$, $L = 7.0$ [λ];
  - Positions: $x_n \in [-L/2, L/2]$, $y_n = \frac{\lambda}{4}$, $n = 1, ..., N$;
  - Excitations: $I_n = 1.0$, $\varphi_n = \frac{-2\pi}{\lambda} x_n sin\,(\phi_s + 90)$; $n = 1, ..., N$;
- **QCTO**
  - Discretization cell dimension: 0.05 [λ] (0.01 [λ] for source mapping);

1.1.1 Results

Transformation grids

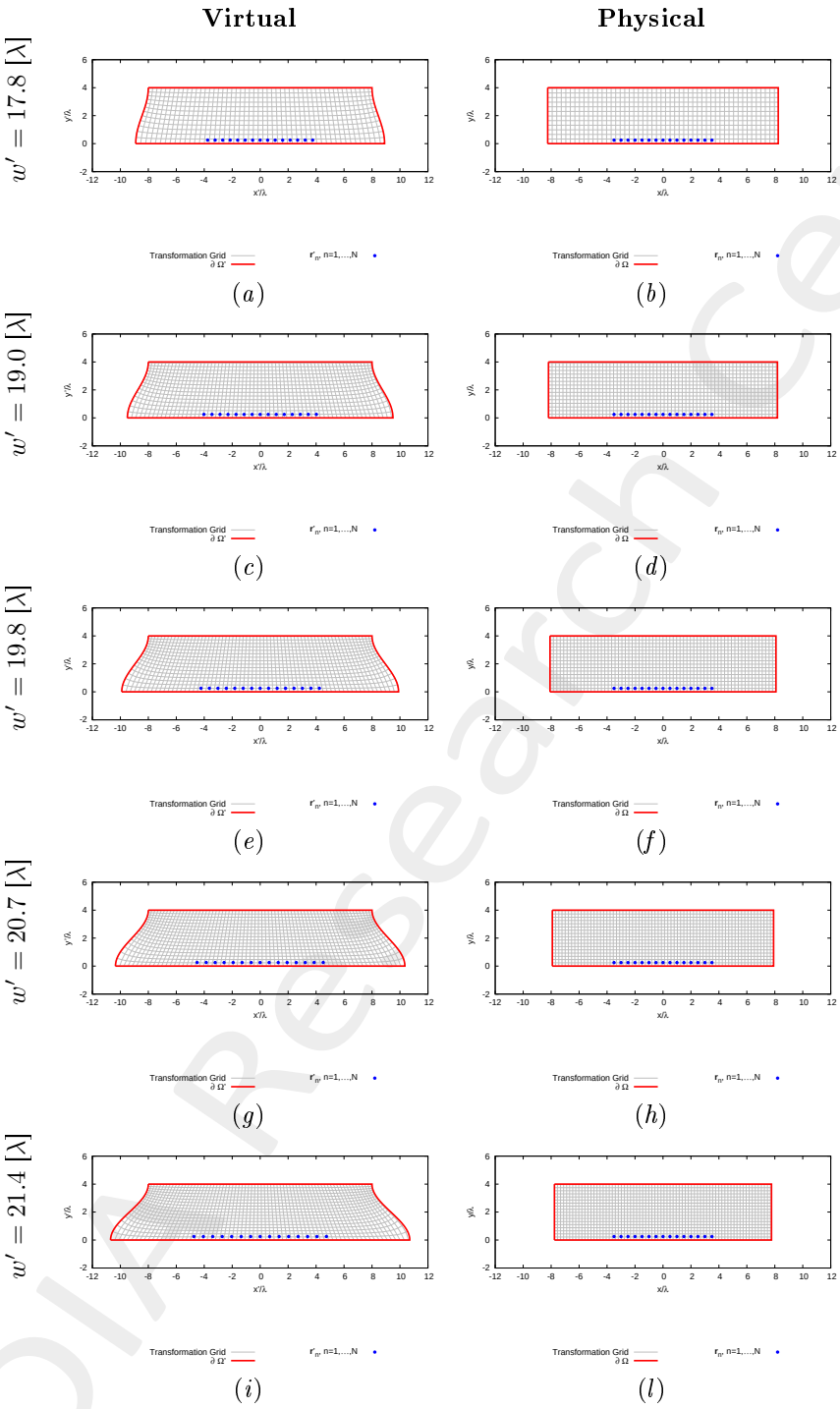

Figure 2: Transformation grids for different values of w'. Physical geometry has been shifted on y by $h/2 = 2.0$ $[\lambda]$.

Resulting aperture of the virtual array (L') - for step 2

- The aperture of the virtual array (L') is computed after mapping the physical array into the virtual space;
- The resulting number of equi-spaced elements is computed as

$$N' = round\left(\frac{L'}{0.5} + 1\right)$$

	Virtual Geometry				**Virtual Array**	
# Test Case	h' [λ]	l' [λ]	t' [λ]	w' [λ]	L' [λ]	N'
1	4.0	0.0	16.0	**17.8**	7.51	**16**
2	4.0	0.0	16.0	**19.0**	8.04	**17**
3	4.0	0.0	16.0	**19.8**	8.47	**18**
4	4.0	0.0	16.0	**20.7**	9.02	**19**
5	4.0	0.0	16.0	**21.4**	9.48	**20**

Table II: Resulting aperture and number of equi-spaced elements of the virtual array after expanding the physical array.

1.2 Step 2: Compressing the virtual array ($N' > N$, $L' > L$ [λ])

Input Parameters

- **Virtual Array**
  - Number of elements, spacing, aperture: $N' = \{16; 17; 18; 19; 20\}$, $d' = \frac{\lambda}{2}$, $L' = \{7.5; 8.0; 8.5; 9.0; 9.5\}$ $[\lambda]$;
  - Positions: $x'_n \in [-L'/2, L'/2]$, $y'_n = \lambda/4$, $n = 1, ..., N'$;
  - Steering angle: $\phi_s = \{90.0;\ 75;\ 60;\ 105;\ 120\}$ $[deg]$;
  - Excitations: $I'_n = 1.0$, $\varphi'_n = \frac{-2\pi}{\lambda} x_n sin\,(\phi_s + 90)$; $n = 1, ..., N'$;
- **Virtual Geometry:** same of step 1;
- **QCTO:** same of step 1.

1.2.1 Results of the Transformation

Transformation grids

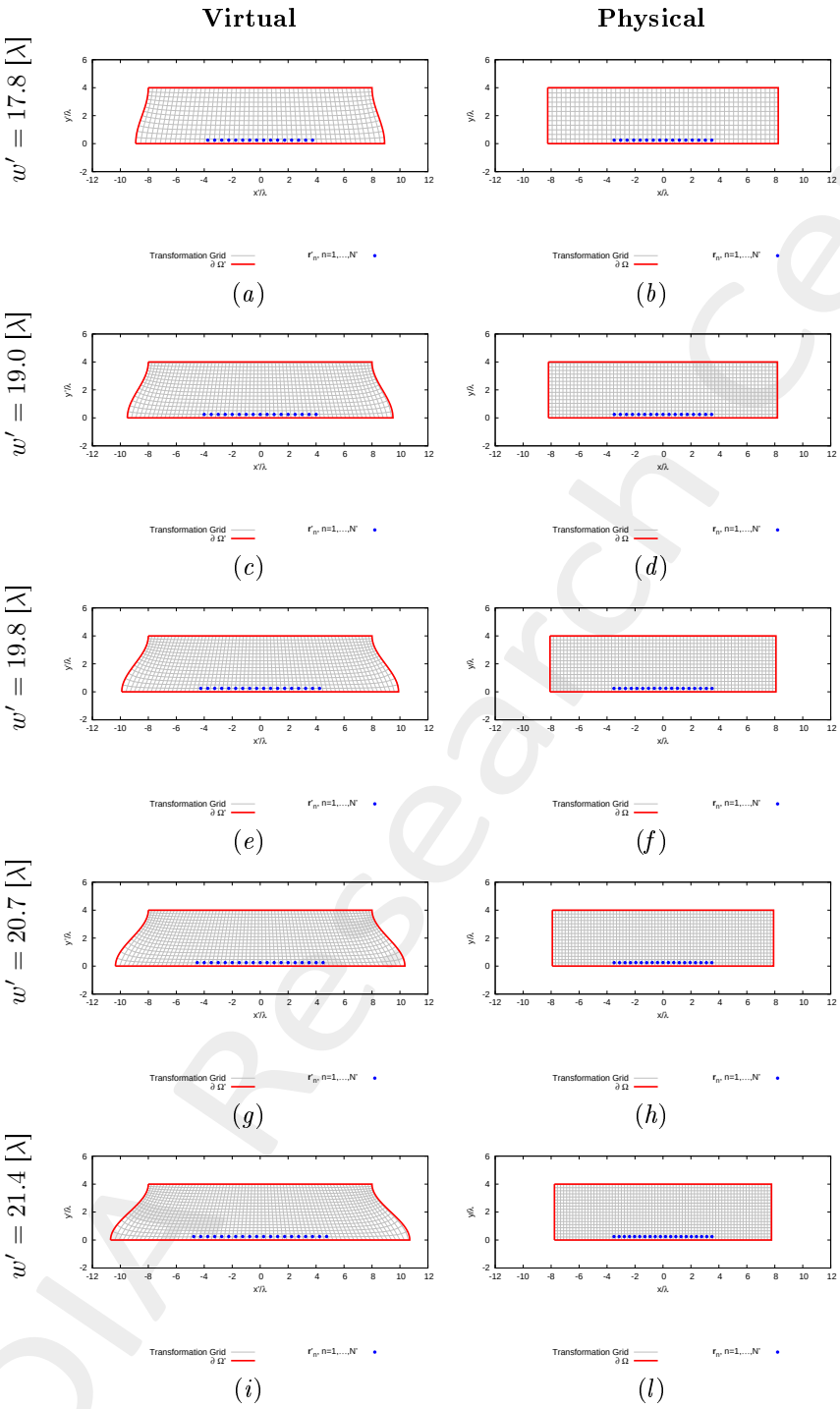

Figure 3: Transformation grids for different values of w'. Physical geometry has been shifted on y by $h/2 = 2.0$ $[\lambda]$.

Lens Permittivity - $w' = 17.8\ [\lambda]$

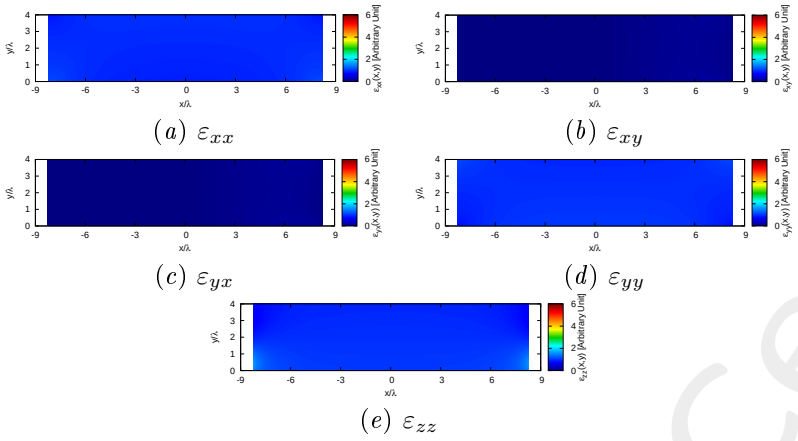

(a) ε_{xx} (b) ε_{xy} (c) ε_{yx} (d) ε_{yy} (e) ε_{zz}

Figure 4: Components of the relative permittivity tensor of the lens.

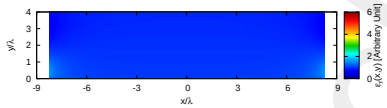

Figure 5: Isotropic approximate permittivity distribution of the lens.

Lens Permittivity - $w' = 19.0\ [\lambda]$

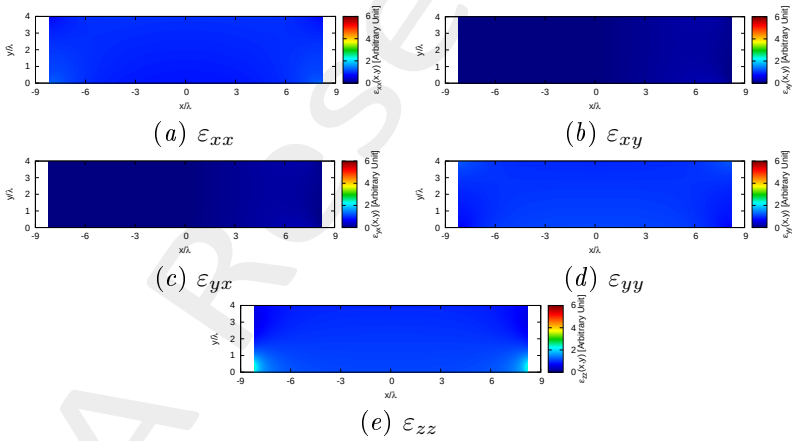

(a) ε_{xx} (b) ε_{xy} (c) ε_{yx} (d) ε_{yy} (e) ε_{zz}

Figure 6: Components of the relative permittivity tensor of the lens.

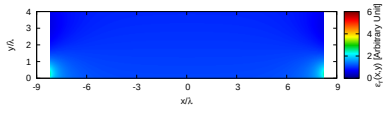

Figure 7: Isotropic approximate permittivity distribution of the lens.

Lens Permittivity - $w' = 19.8\ [\lambda]$

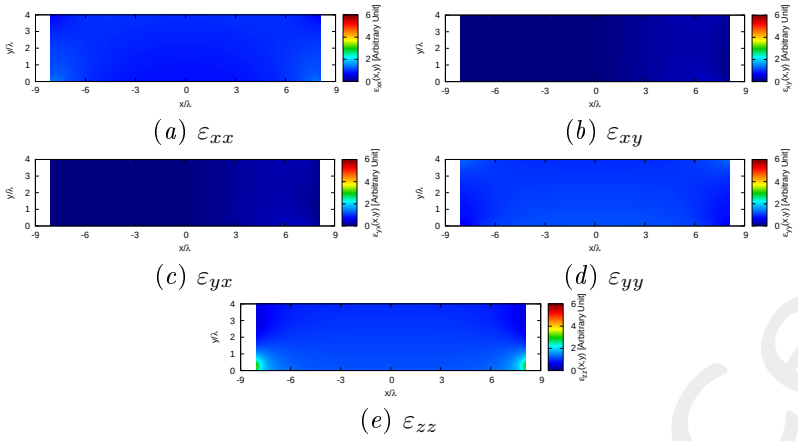

(a) ε_{xx} (b) ε_{xy} (c) ε_{yx} (d) ε_{yy} (e) ε_{zz}

Figure 8: Components of the relative permittivity tensor of the lens.

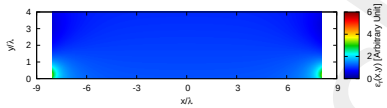

Figure 9: Isotropic approximate permittivity distribution of the lens.

Lens Permittivity - $w' = 20.7\ [\lambda]$

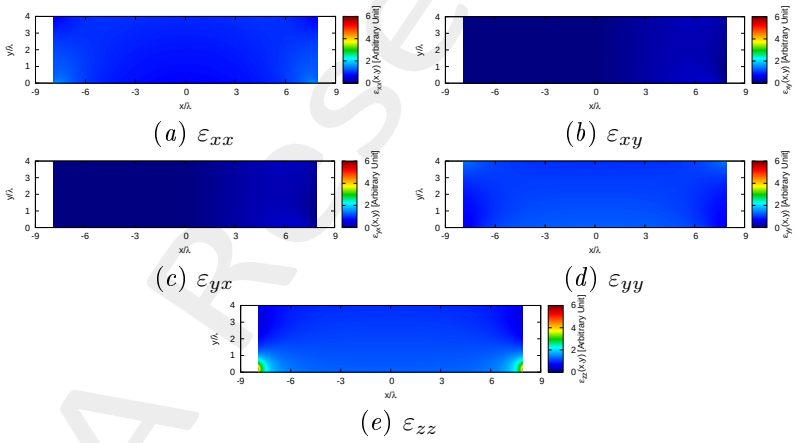

(a) ε_{xx} (b) ε_{xy} (c) ε_{yx} (d) ε_{yy} (e) ε_{zz}

Figure 10: Components of the relative permittivity tensor of the lens.

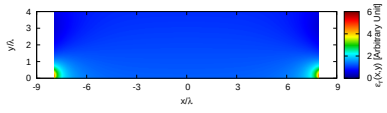

Figure 11: Isotropic approximate permittivity distribution of the lens.

Lens Permittivity - $w' = 21.4\ [\lambda]$

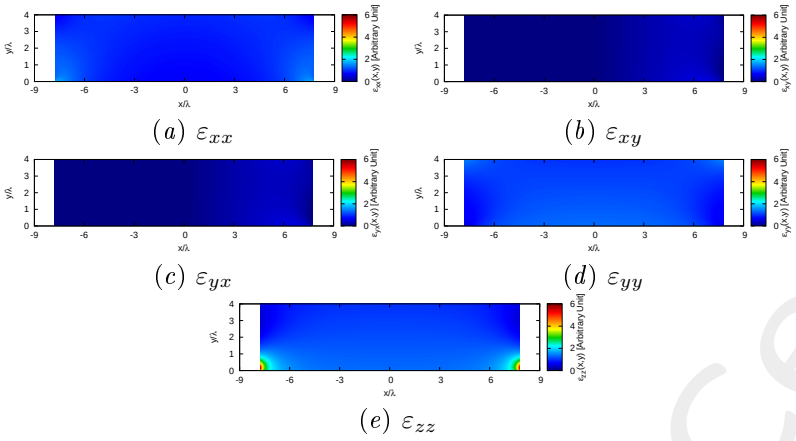

Figure 12: Components of the relative permittivity tensor of the lens.

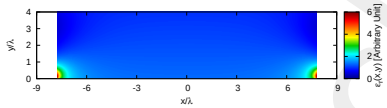

Figure 13: Isotropic approximate permittivity distribution of the lens.

1.2.2 Far-Field Patterns ($\phi_s = 90$ [deg], $f = 600$ [MHz])

Anisotropic Lens

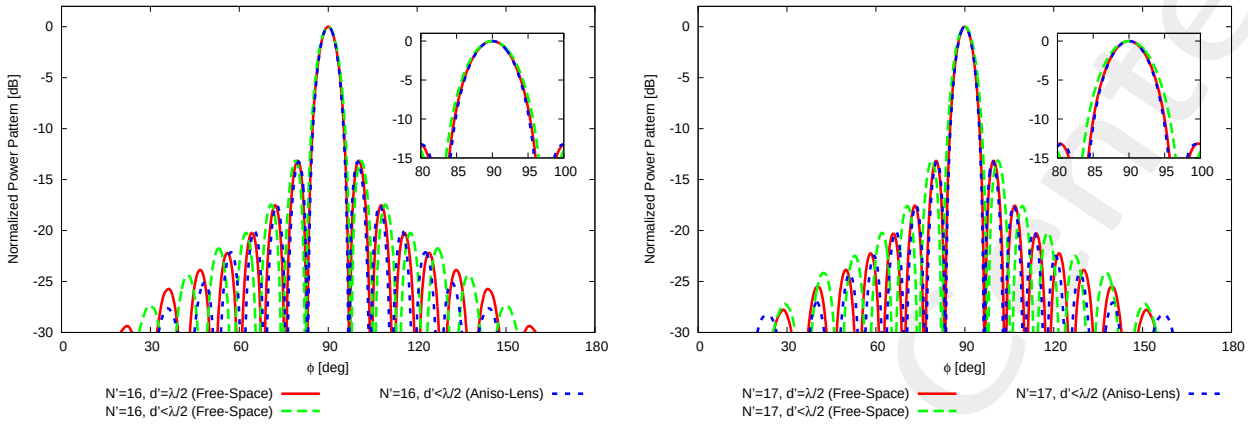

(a) $w' = 17.8$ $[\lambda]$, $N' = 16$

(b) $w' = 19.0$ $[\lambda]$, $N' = 17$

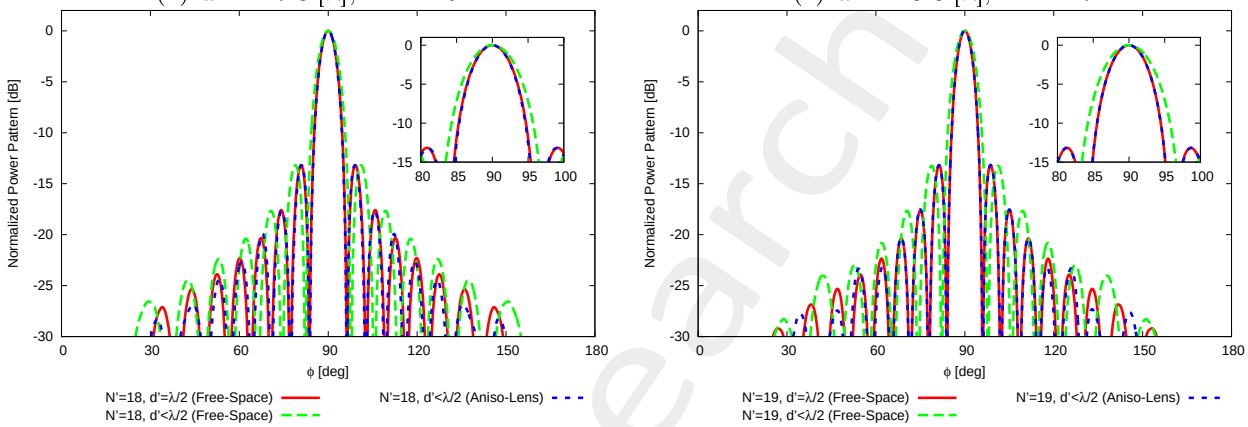

(c) $w' = 19.8$ $[\lambda]$, $N' = 18$

(d) $w' = 20.7$ $[\lambda]$, $N' = 19$

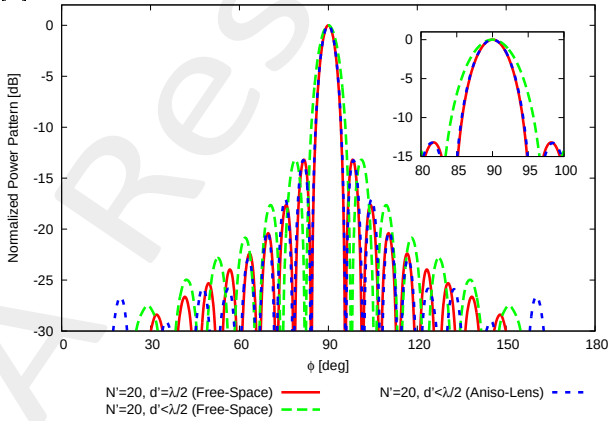

(e) $w' = 21.4$ $[\lambda]$, $N' = 20$

Figure 14: Far field pattern comparison for different values of w'.

1.2.3 Far-Field Patterns ($\phi_s = 75$ [deg], $f = 600$ [MHz])

Anisotropic Lens

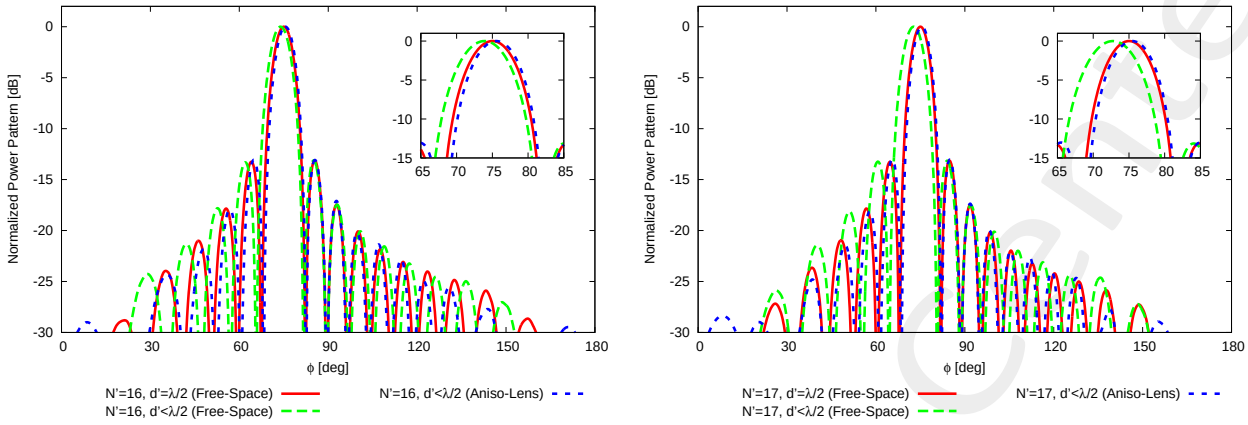

(a) $w' = 17.8$ $[\lambda]$, $N' = 16$

(b) $w' = 19.0$ $[\lambda]$, $N' = 17$

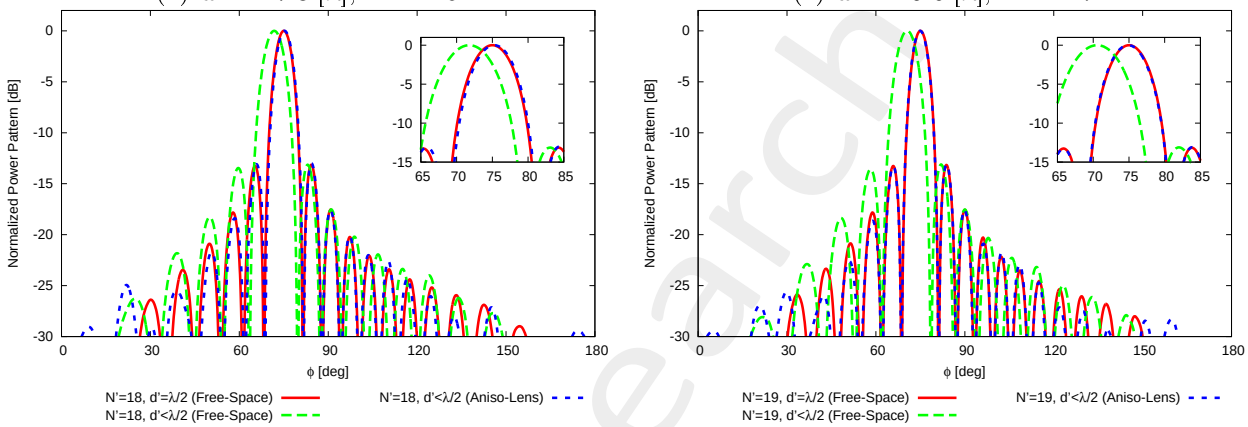

(c) $w' = 19.8$ $[\lambda]$, $N' = 18$

(d) $w' = 20.7$ $[\lambda]$, $N' = 19$

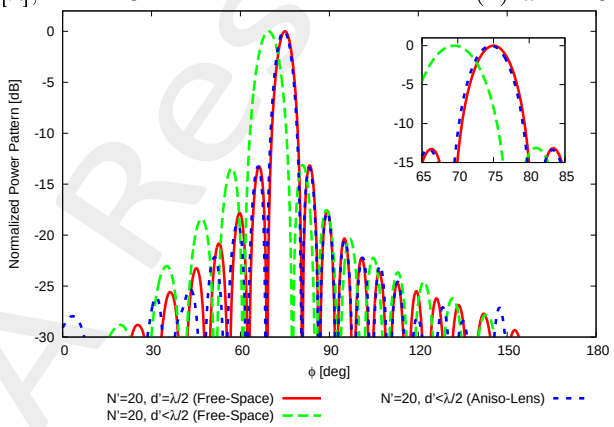

(e) $w' = 21.4$ $[\lambda]$, $N' = 20$

Figure 15: Far field pattern comparison for different values of w'.

1.2.4 Far-Field Patterns ($\phi_s = 60$ [deg], $f = 600$ [MHz])

Anisotropic Lens

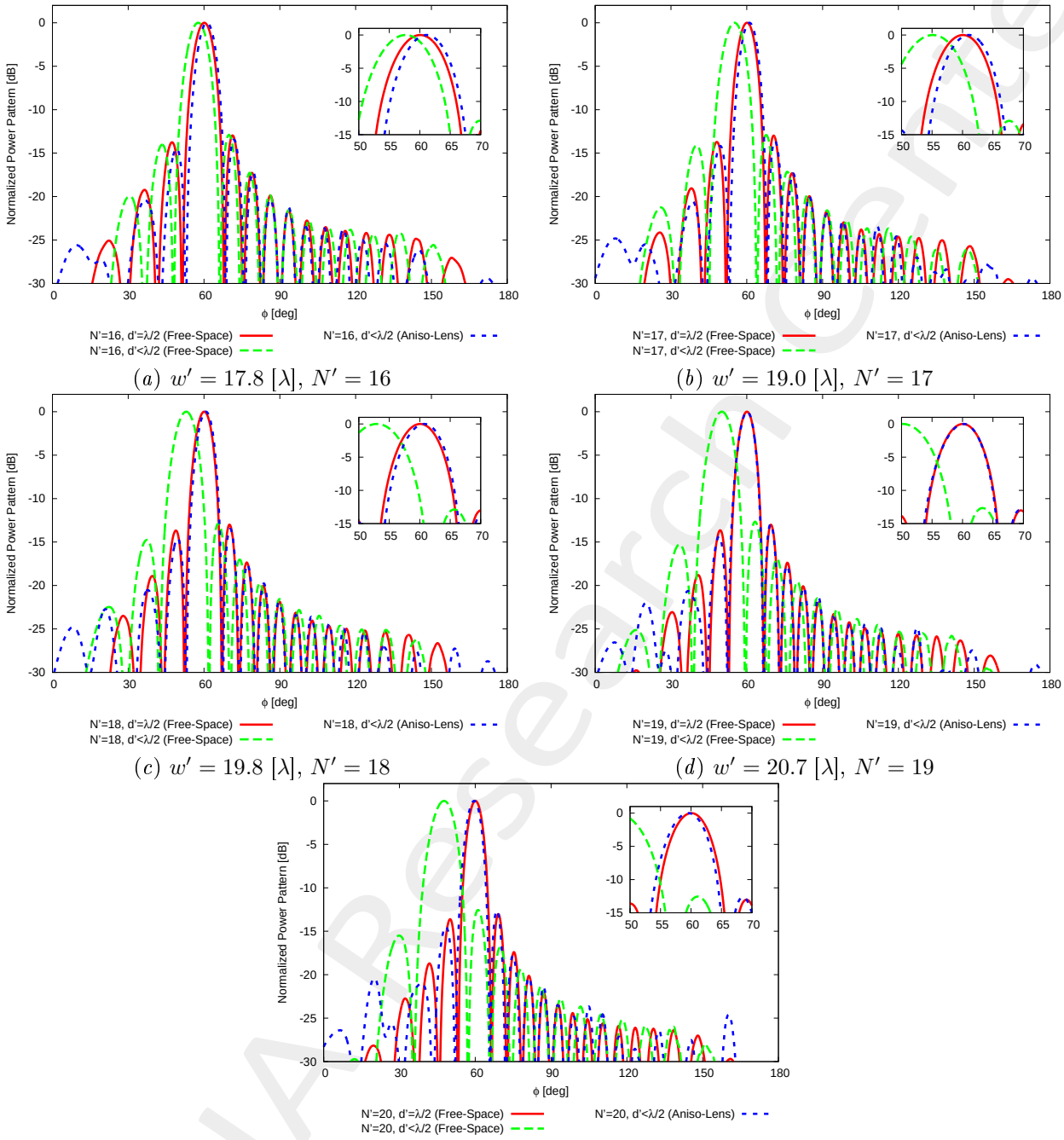

(a) $w' = 17.8$ $[\lambda]$, $N' = 16$

(b) $w' = 19.0$ $[\lambda]$, $N' = 17$

(c) $w' = 19.8$ $[\lambda]$, $N' = 18$

(d) $w' = 20.7$ $[\lambda]$, $N' = 19$

(e) $w' = 21.4$ $[\lambda]$, $N' = 20$

Figure 16: Far field pattern comparison for different values of w'.

1.2.5 Far-Field Patterns ($\phi_s = 95$ [deg], $f = 600$ [MHz])

Anisotropic Lens

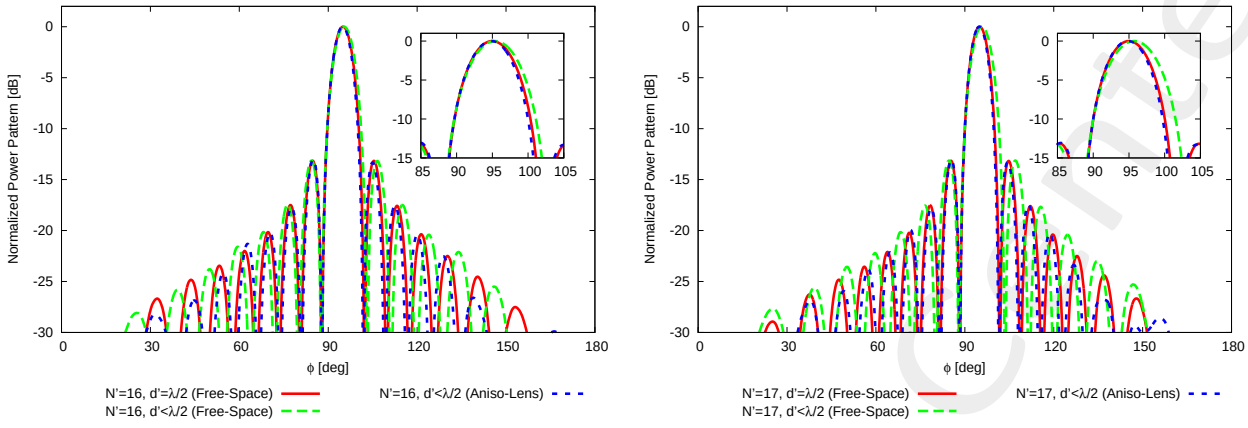

(a) $w' = 17.8$ $[\lambda]$, $N' = 16$

(b) $w' = 19.0$ $[\lambda]$, $N' = 17$

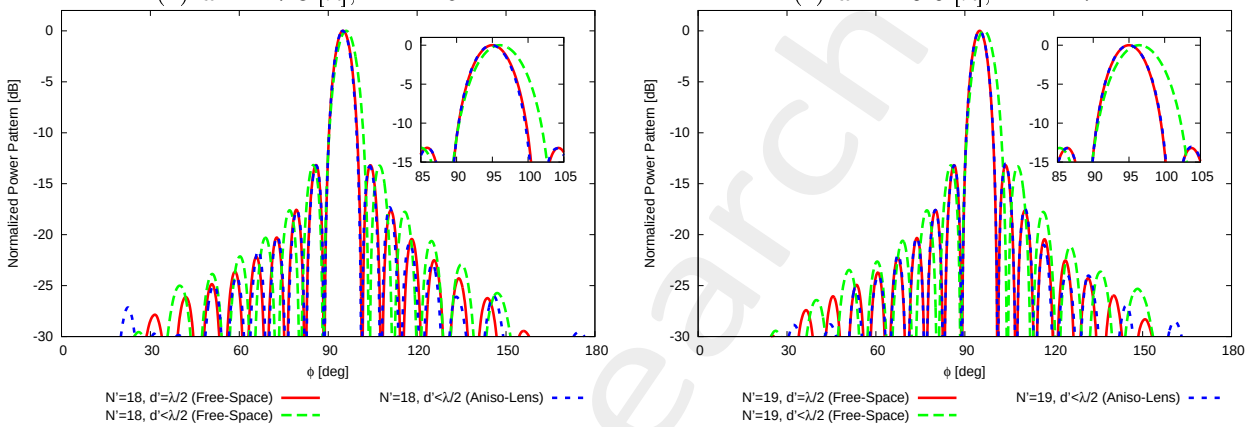

(c) $w' = 19.8$ $[\lambda]$, $N' = 18$

(d) $w' = 20.7$ $[\lambda]$, $N' = 19$

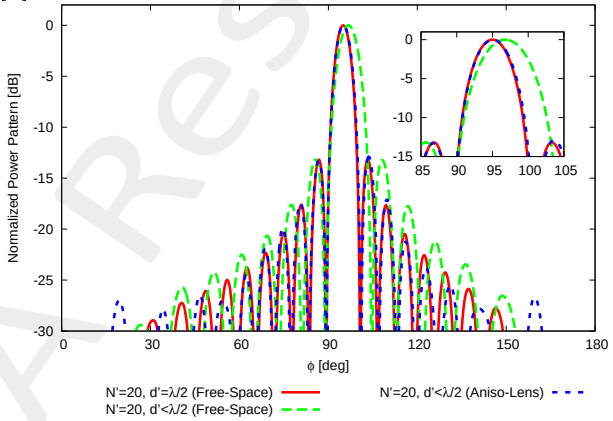

(e) $w' = 21.4$ $[\lambda]$, $N' = 20$

Figure 17: Far field pattern comparison for different values of w'.

1.2.6 Far-Field Patterns ($\phi_s = 100$ [deg], $f = 600$ [MHz])

Anisotropic Lens

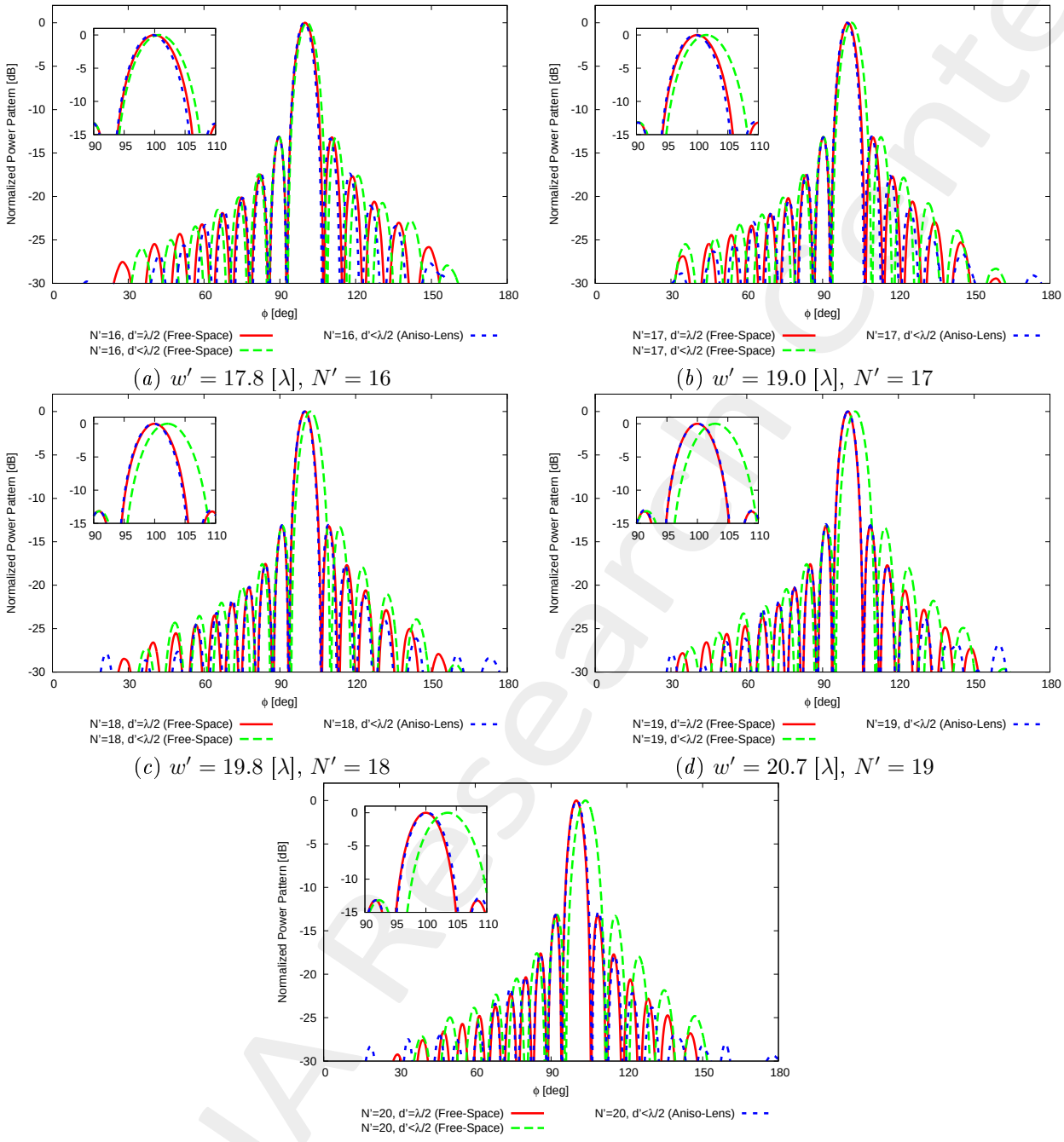

(a) $w' = 17.8$ $[\lambda]$, $N' = 16$

(b) $w' = 19.0$ $[\lambda]$, $N' = 17$

(c) $w' = 19.8$ $[\lambda]$, $N' = 18$

(d) $w' = 20.7$ $[\lambda]$, $N' = 19$

(e) $w' = 21.4$ $[\lambda]$, $N' = 20$

Figure 18: Far field pattern comparison for different values of w'.

1.2.7 Far-Field Patterns ($\phi_s = 105$ [deg], $f = 600$ [MHz])

Anisotropic Lens

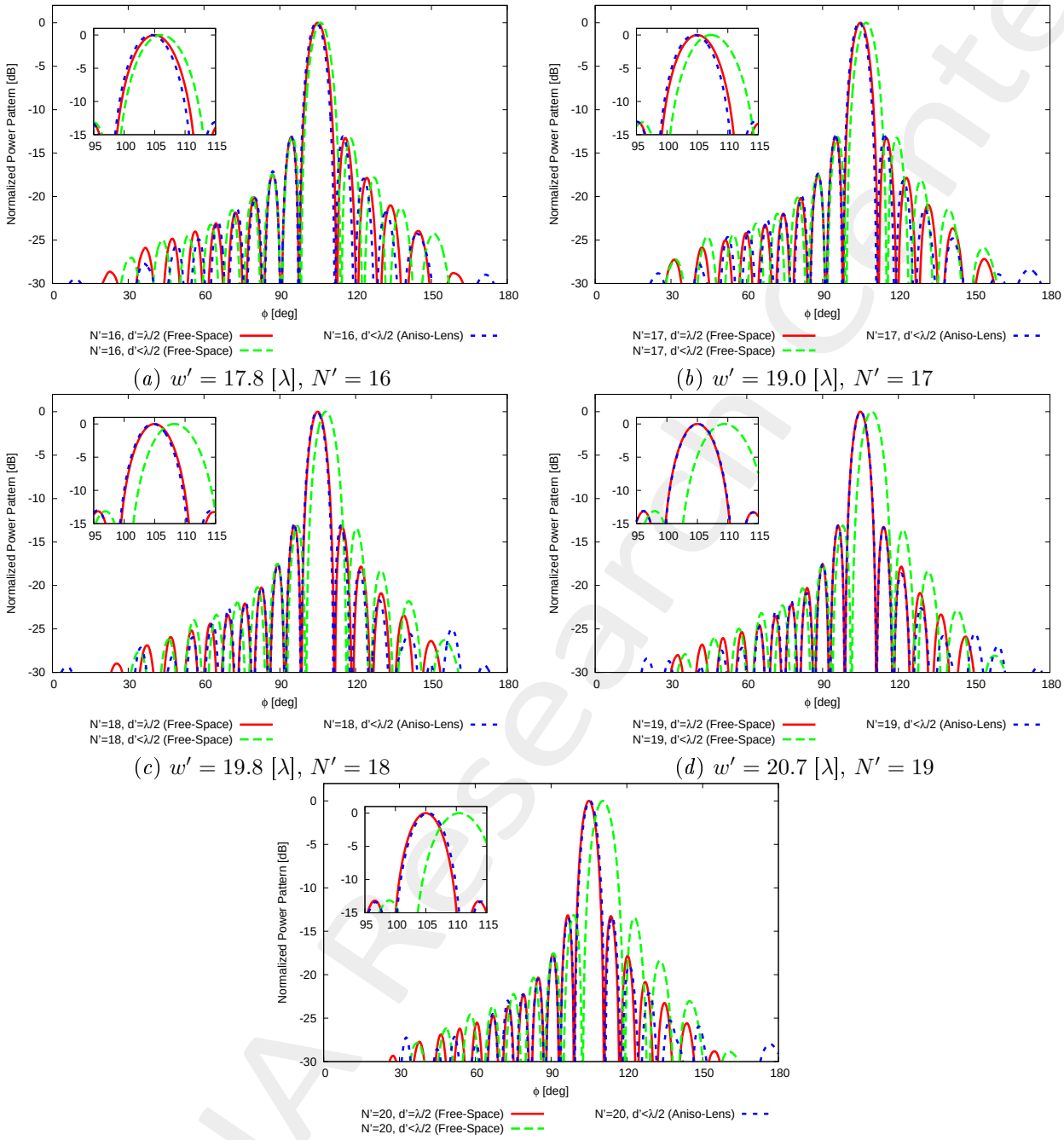

(a) $w' = 17.8$ $[\lambda]$, $N' = 16$

(b) $w' = 19.0$ $[\lambda]$, $N' = 17$

(c) $w' = 19.8$ $[\lambda]$, $N' = 18$

(d) $w' = 20.7$ $[\lambda]$, $N' = 19$

(e) $w' = 21.4$ $[\lambda]$, $N' = 20$

Figure 19: Far field pattern comparison for different values of w'.

1.2.8 Far-Field Patterns ($\phi_s = 110$ [deg], $f = 600$ [MHz])

Anisotropic Lens

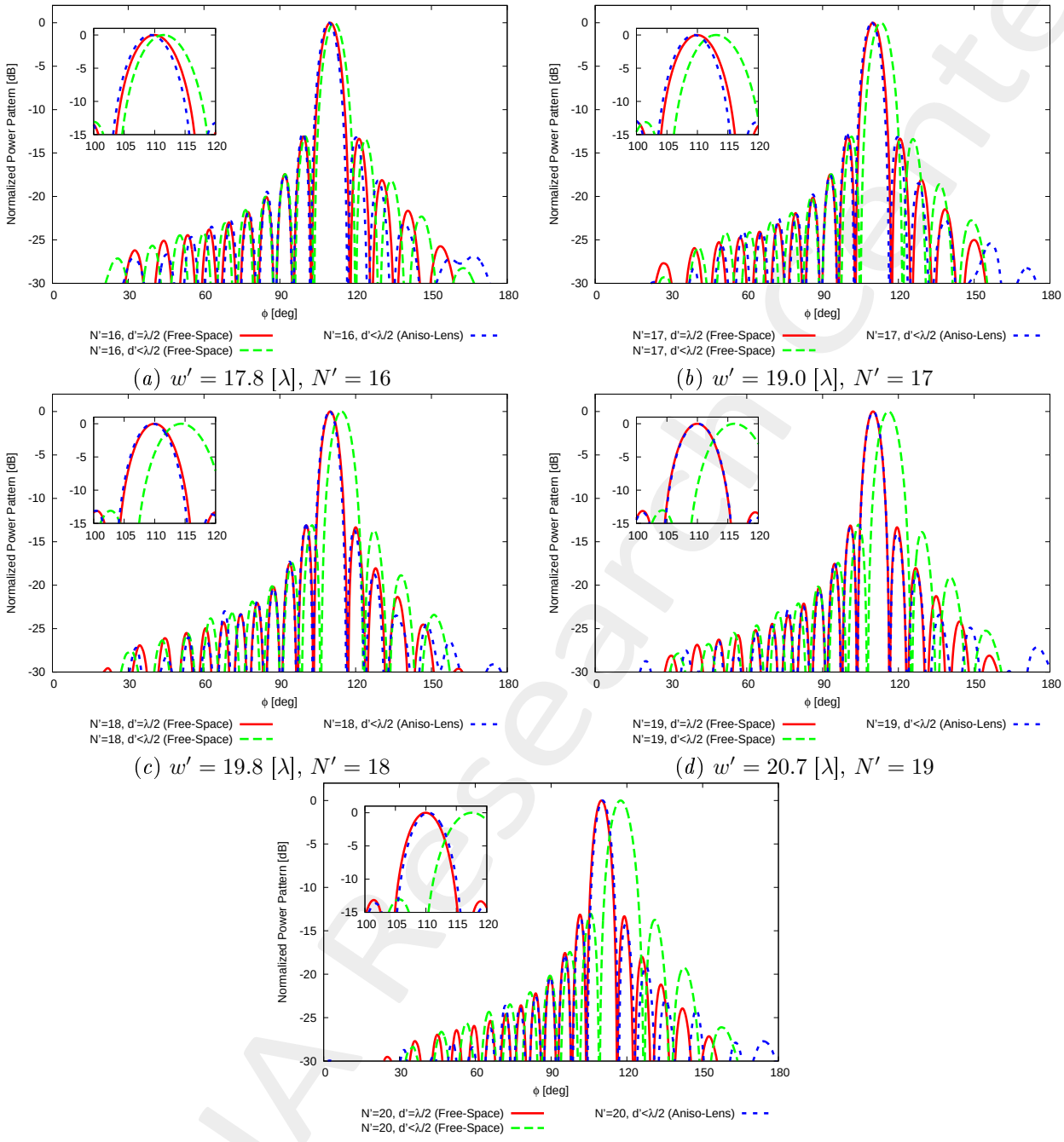

(a) $w' = 17.8$ $[\lambda]$, $N' = 16$

(b) $w' = 19.0$ $[\lambda]$, $N' = 17$

(c) $w' = 19.8$ $[\lambda]$, $N' = 18$

(d) $w' = 20.7$ $[\lambda]$, $N' = 19$

(e) $w' = 21.4$ $[\lambda]$, $N' = 20$

Figure 20: Far field pattern comparison for different values of w'.

1.2.9 Far-Field Patterns ($\phi_s = 120$ [deg], $f = 600$ [MHz])

Anisotropic Lens

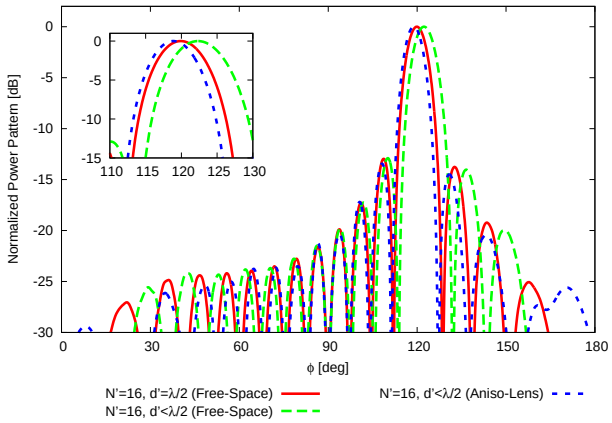

(a) $w' = 17.8$ $[\lambda]$, $N' = 16$

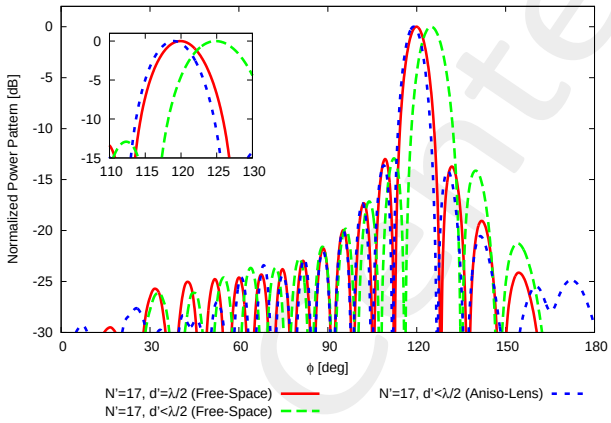

(b) $w' = 19.0$ $[\lambda]$, $N' = 17$

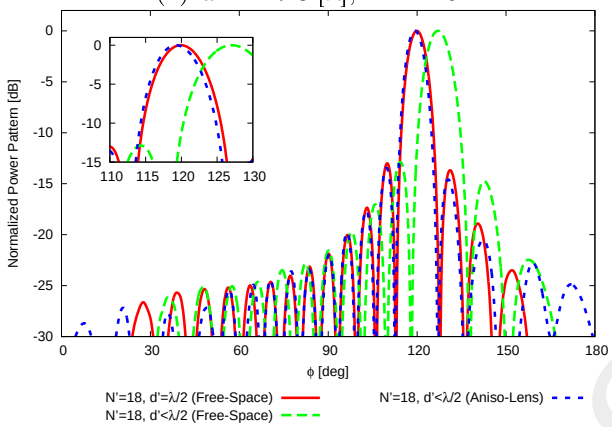

(c) $w' = 19.8$ $[\lambda]$, $N' = 18$

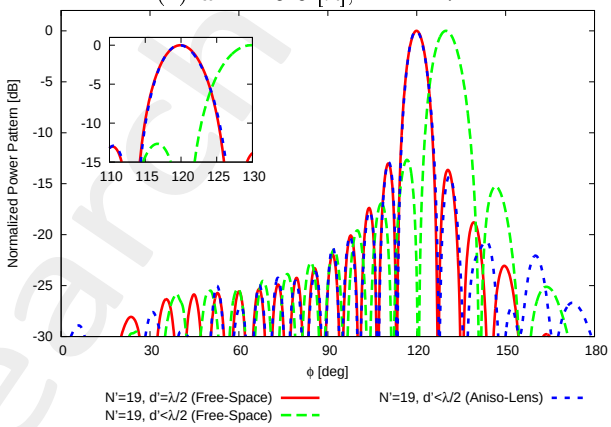

(d) $w' = 20.7$ $[\lambda]$, $N' = 19$

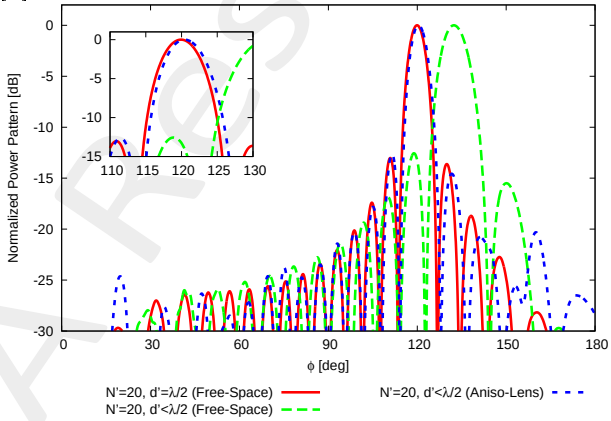

(e) $w' = 21.4$ $[\lambda]$, $N' = 20$

Figure 21: Far field pattern comparison for different values of w'.

1.3 Source Inversion (SI)

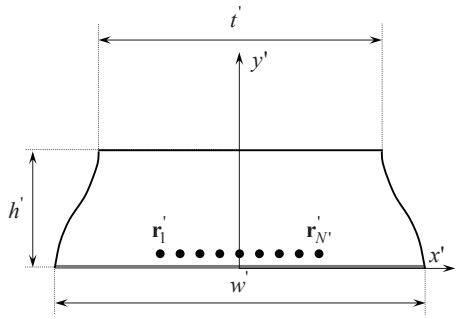

(a) Virtual

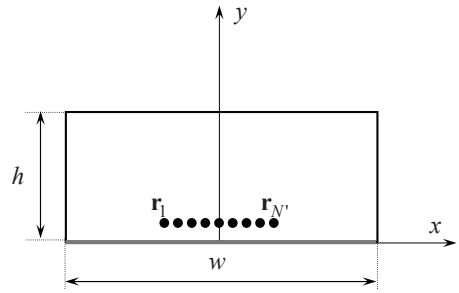

(b) Physical-Dense

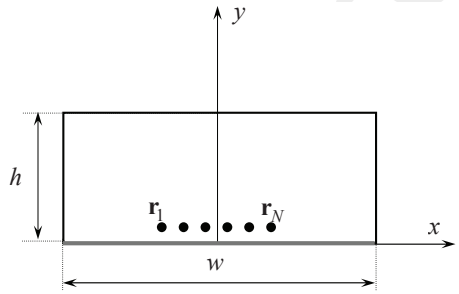

(c) Physical-SI

Figure 22: Geometry for (a) the virtual array in free-space, (b) the "physical-dense" array inside the lens and (c) the physical-SI array inside the lens.

Parameters

- Before SI
  - Number of elements: $N' = \{16; 17; 18; 19; 20\}$, $d' < \lambda/2$;
- After SI
  - Number of elements after SI: $N = 15$, $d = \frac{\lambda}{2}$;
  - Aperture: $L = 7.0$;
- Radius of the observation domain: $r_{SI} = 400$ $[\lambda]$;
- Number of field sampling points: $n_{SI} = 1000$.

1.3.1 Results of the SI

Synthesized Excitations ($\phi_s = 90$ [deg], $f = 600$ [MHz])

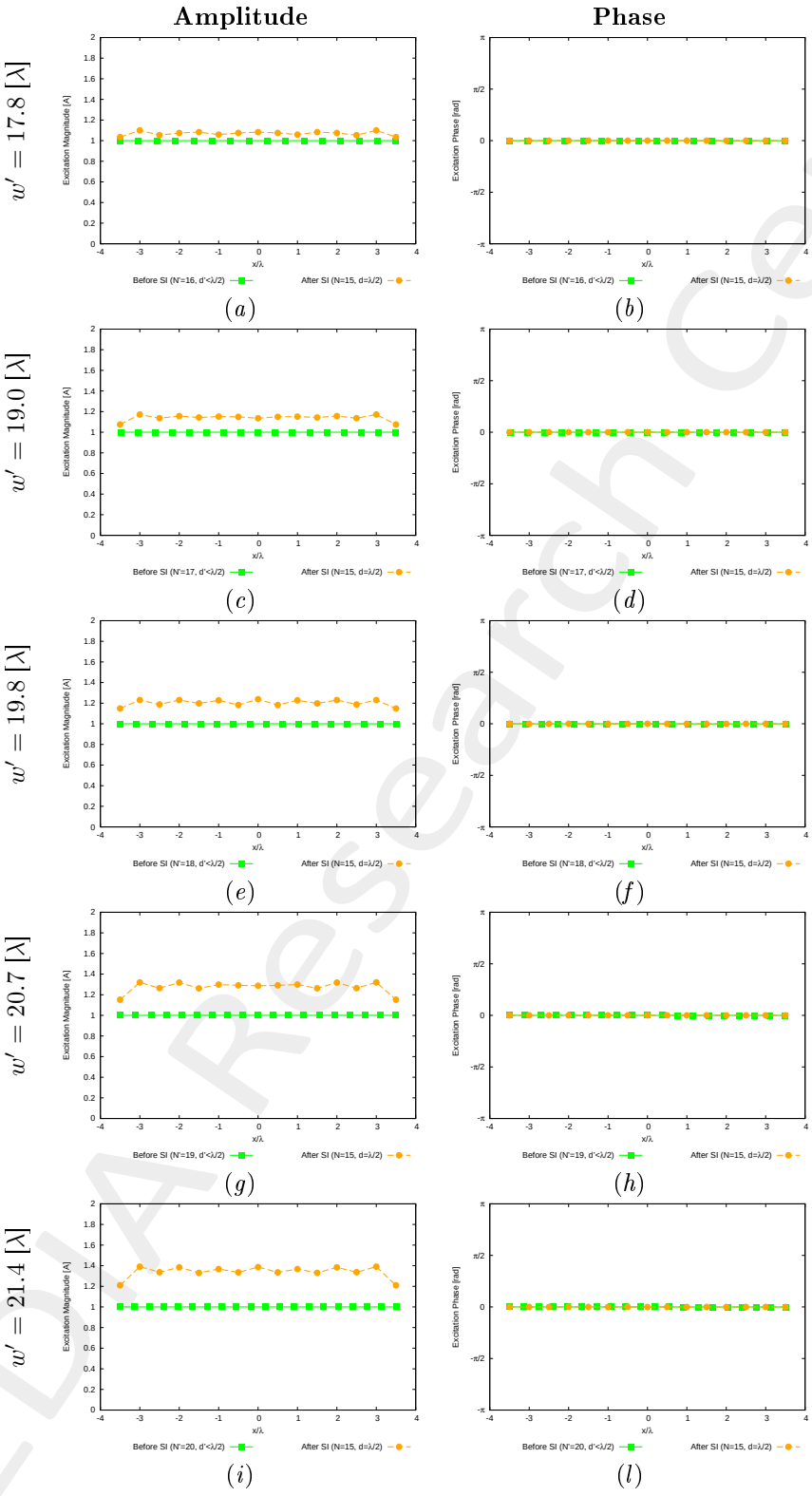

Figure 23: $\phi_s = 90$ [deg], $f = 600$ [MHz] - Synthesized excitations through SI.

Synthesized Excitations ($\phi_s = 75$ [deg], $f = 600$ [MHz])

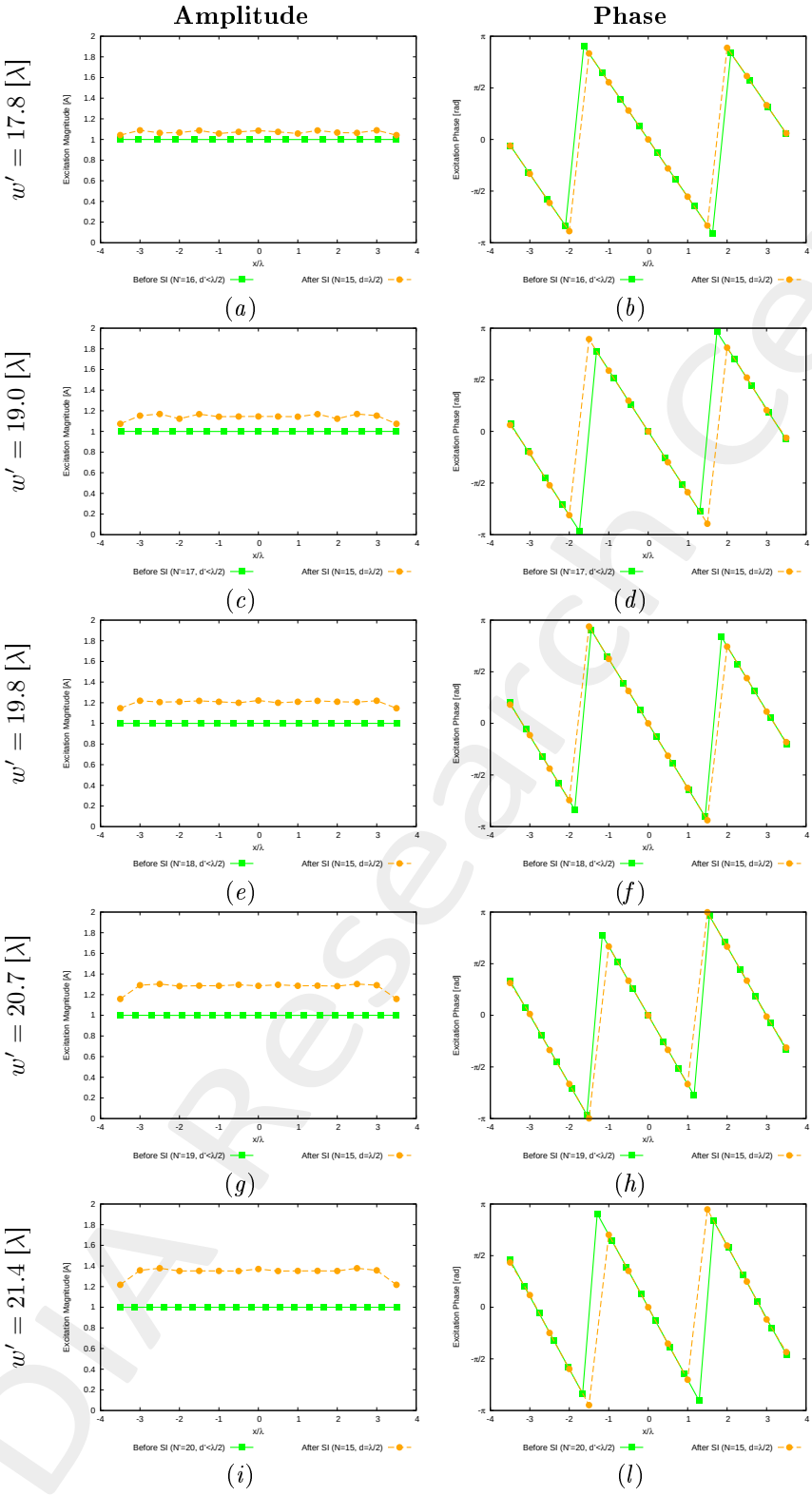

Figure 24: $\phi_s = 75$ [deg], $f = 600$ [MHz] - Synthesized excitations through SI.

Synthesized Excitations ($\phi_s = 60$ [deg], $f = 600$ [MHz])

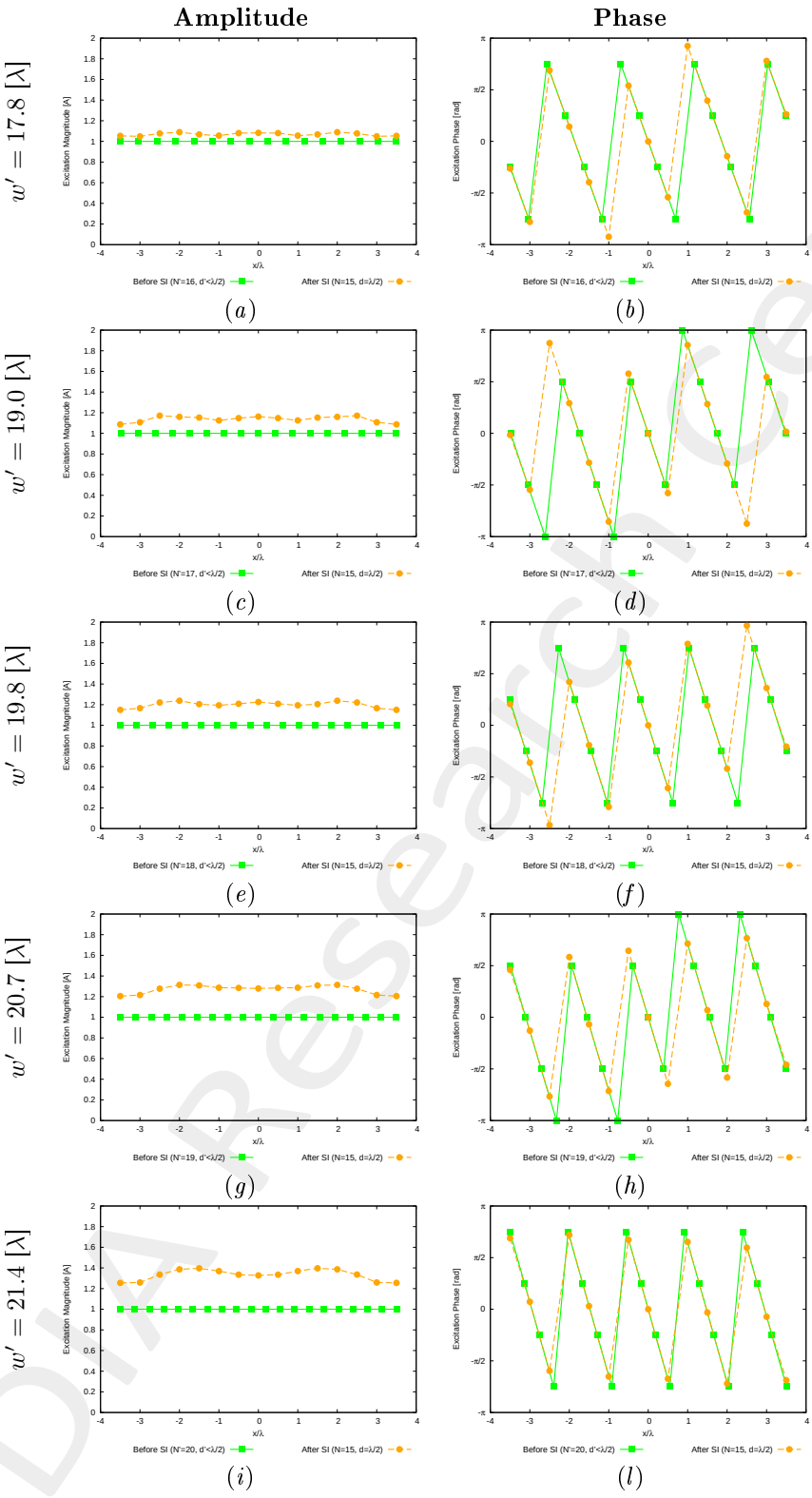

Figure 25: $\phi_s = 60$ [deg], $f = 600$ [MHz] - Synthesized excitations through SI.

Synthesized Excitations ($\phi_s = 95$ [deg], $f = 600$ [MHz])

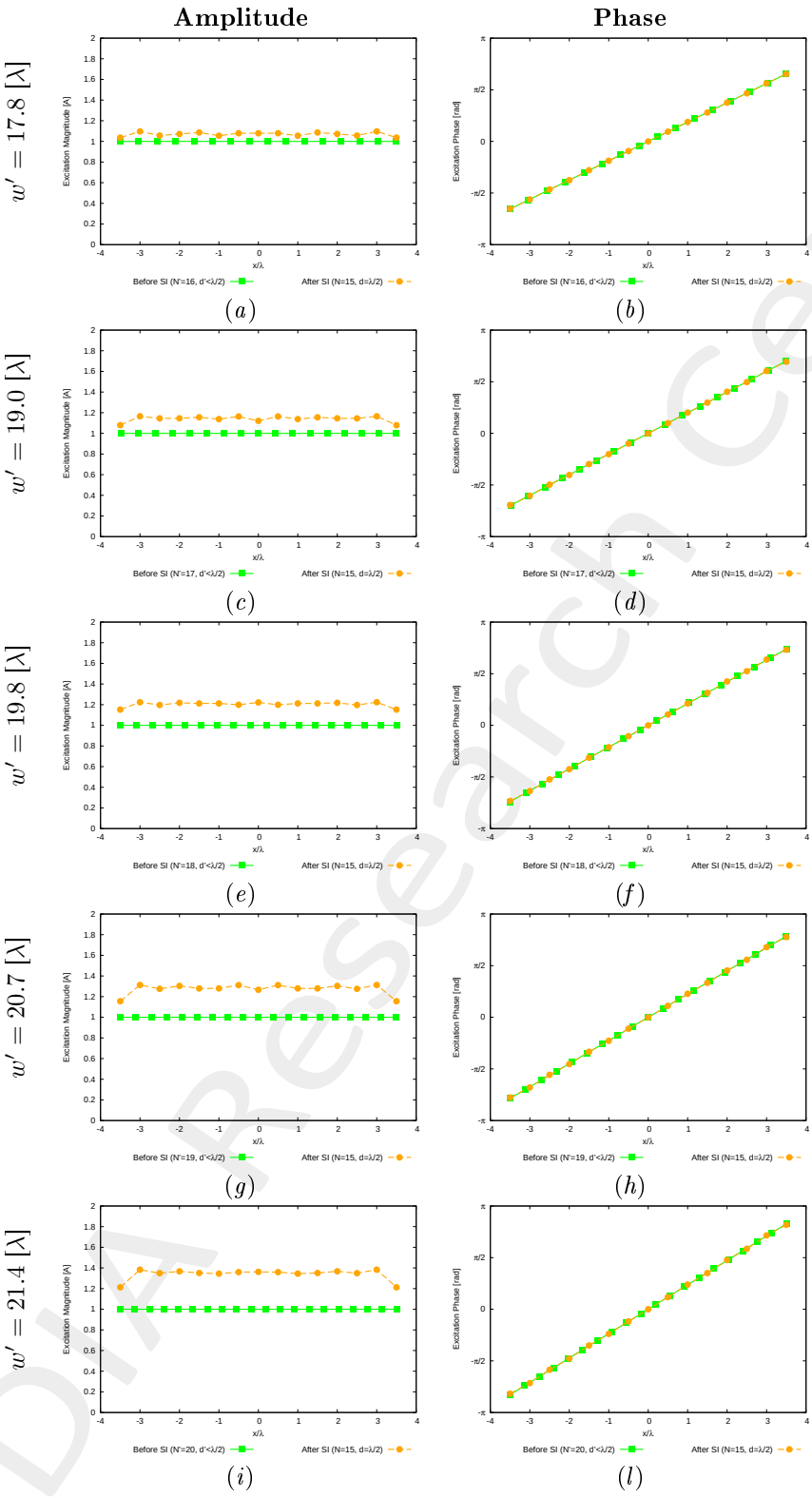

Figure 26: $\phi_s = 95$ [deg], $f = 600$ [MHz] - Synthesized excitations through SI.

Synthesized Excitations ($\phi_s = 100$ [deg], $f = 600$ [MHz])

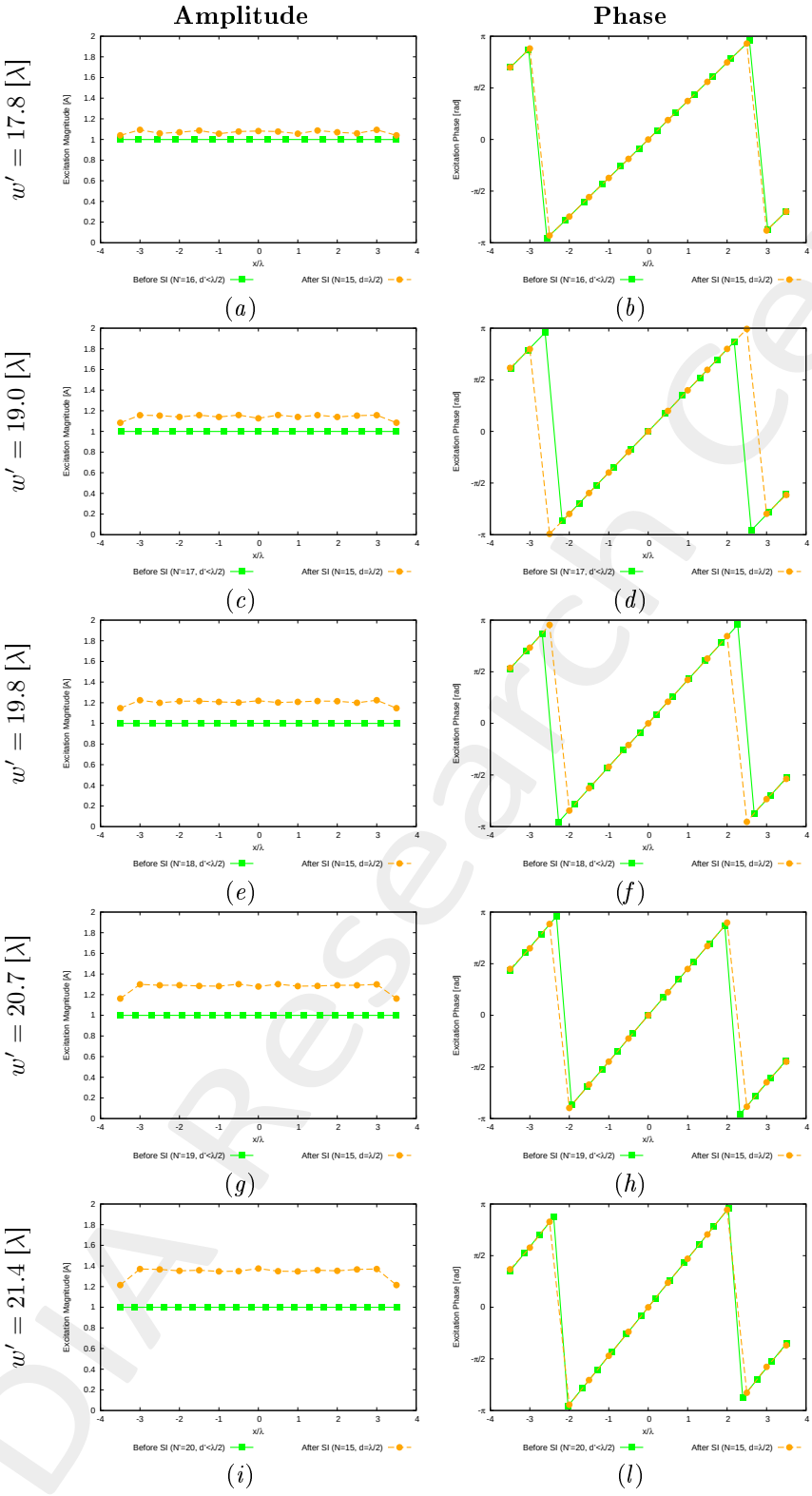

Figure 27: $\phi_s = 100$ [deg], $f = 600$ [MHz] - Synthesized excitations through SI.

Synthesized Excitations ($\phi_s = 105$ [deg], $f = 600$ [MHz])

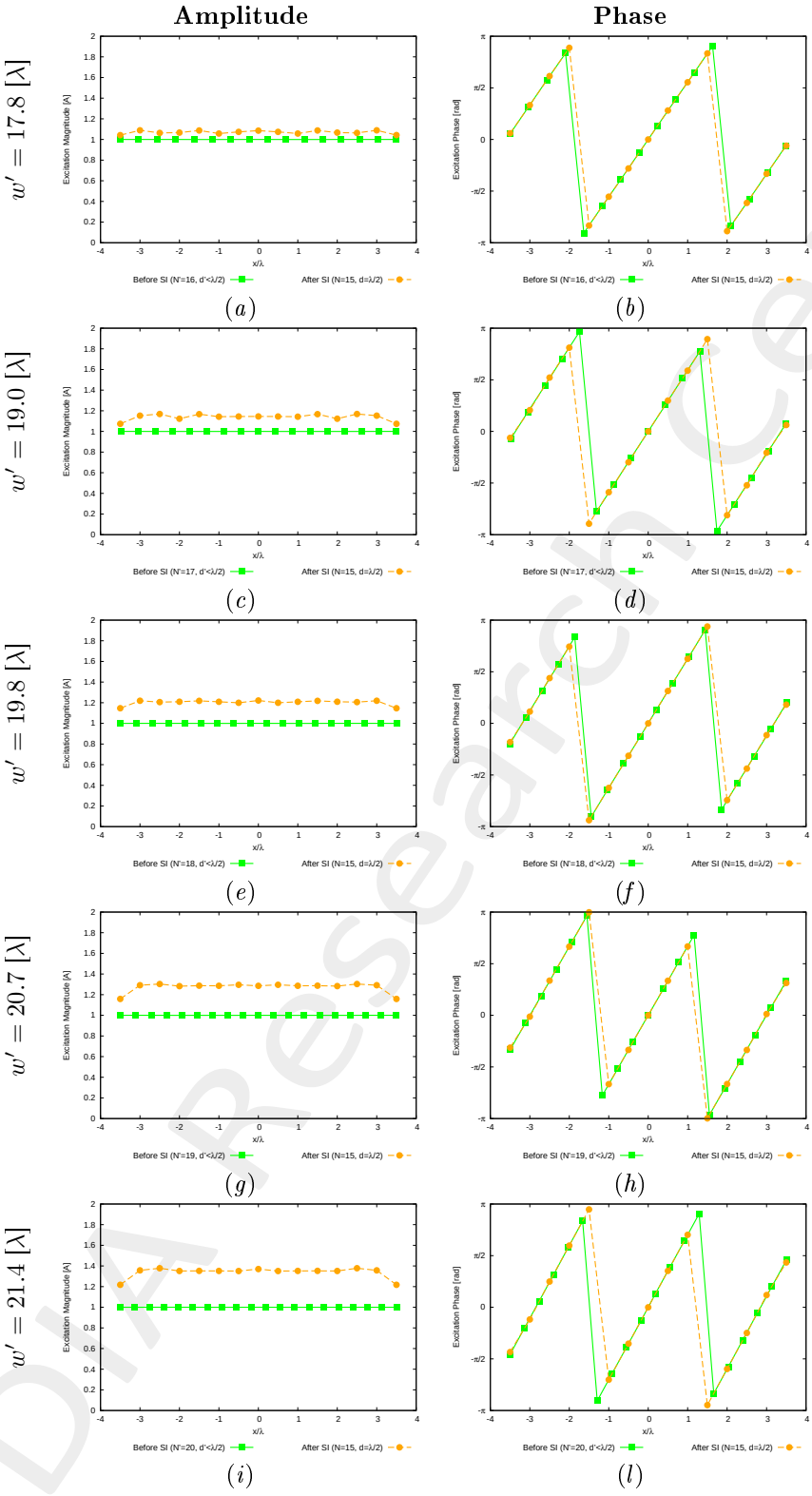

Figure 28: $\phi_s = 105$ [deg], $f = 600$ [MHz] - Synthesized excitations through SI.

Synthesized Excitations ($\phi_s = 110$ [deg], $f = 600$ [MHz])

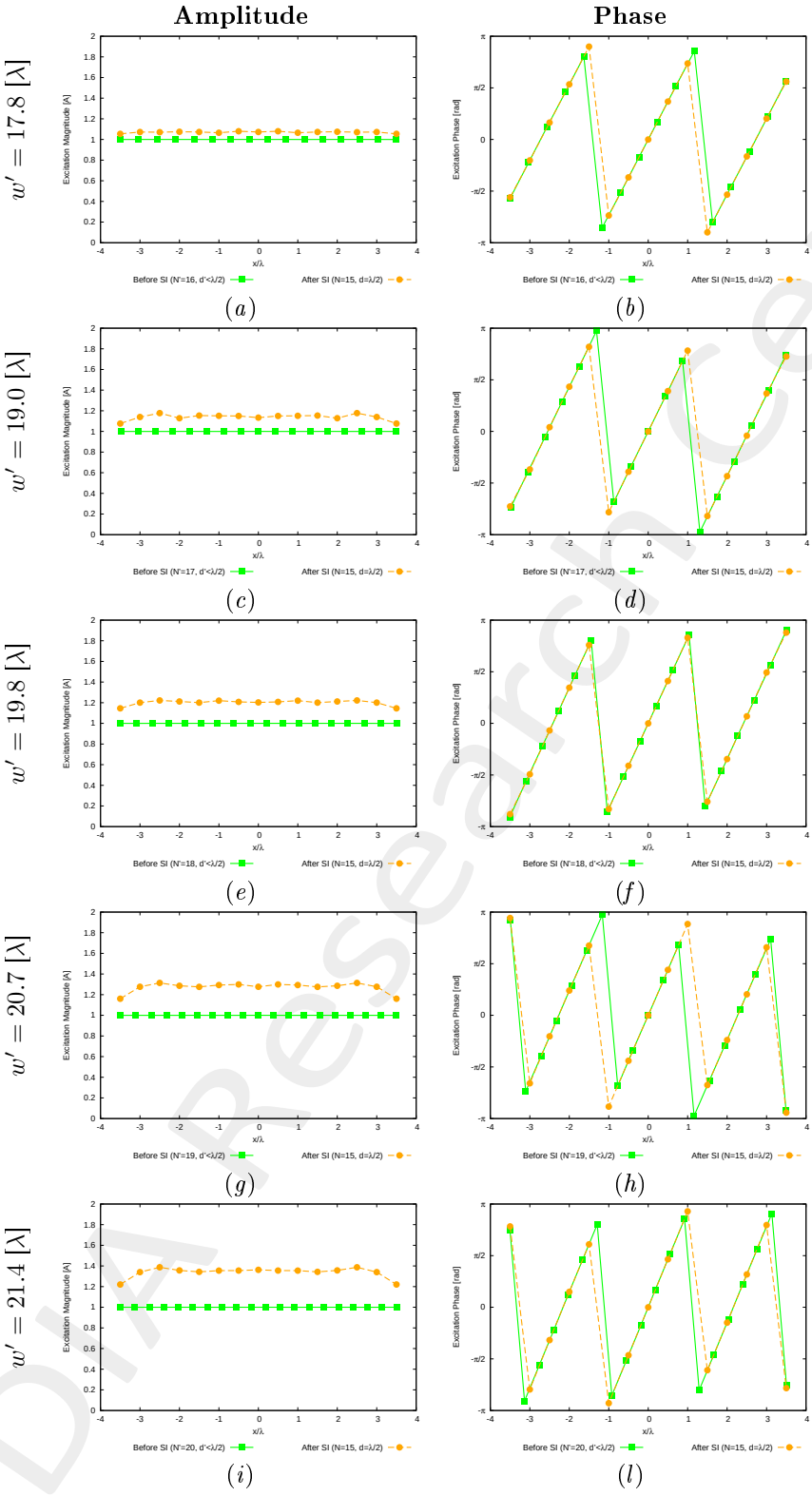

Figure 29: $\phi_s = 110$ [deg], $f = 600$ [MHz] - Synthesized excitations through SI.

Synthesized Excitations ($\phi_s = 120$ [deg], $f = 600$ [MHz])

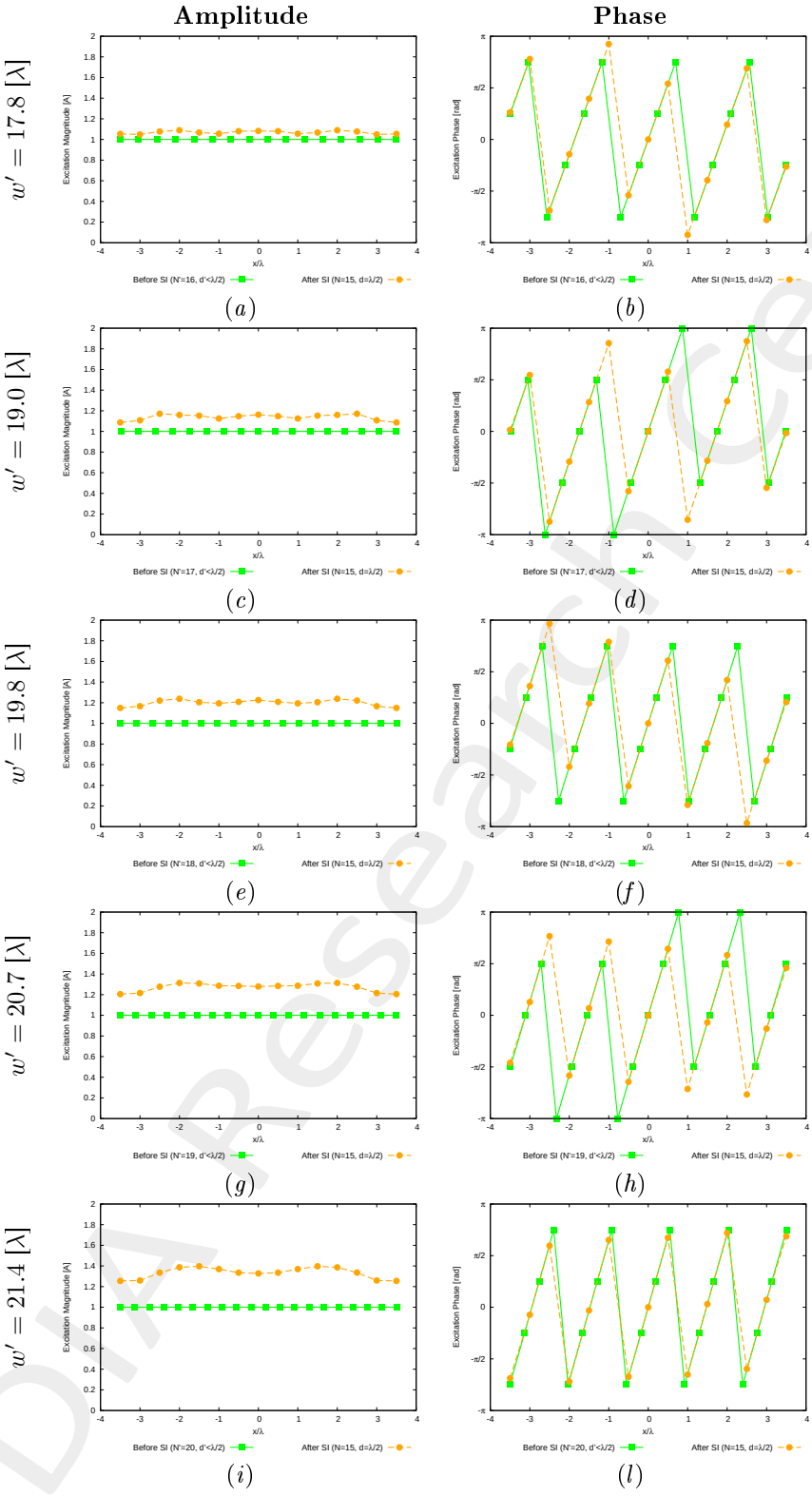

Figure 30: $\phi_s = 120$ [deg], $f = 600$ [MHz] - Synthesized excitations through SI.

1.3.2 Far-Field Patterns ($\phi_s = 90$ [deg], $f = 600$ [MHz])

Anisotropic Lens

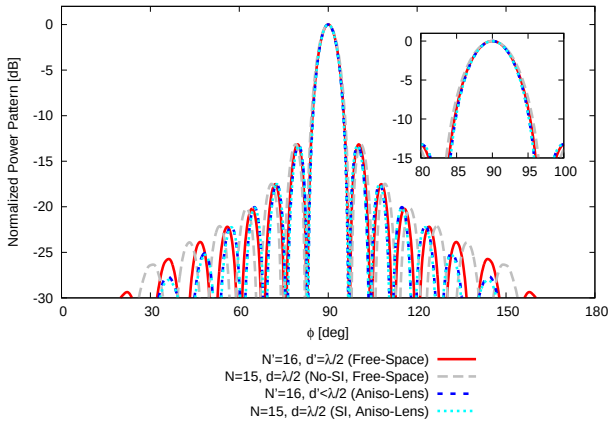

(a) $w' = 17.8$ $[\lambda]$, $N' = 16$

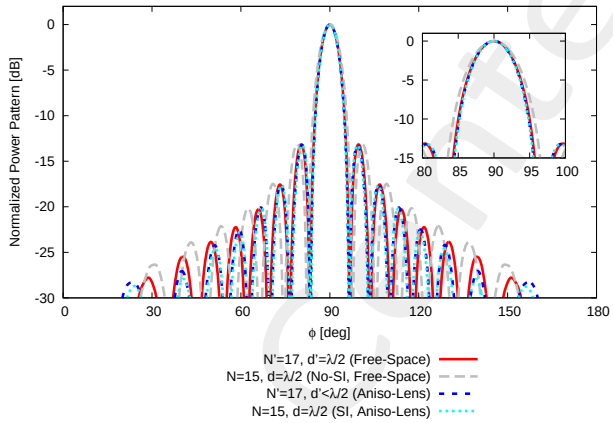

(b) $w' = 19.0$ $[\lambda]$, $N' = 17$

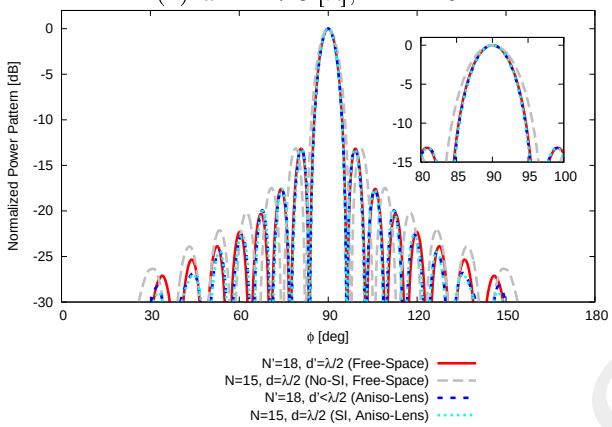

(c) $w' = 19.8$ $[\lambda]$, $N' = 18$

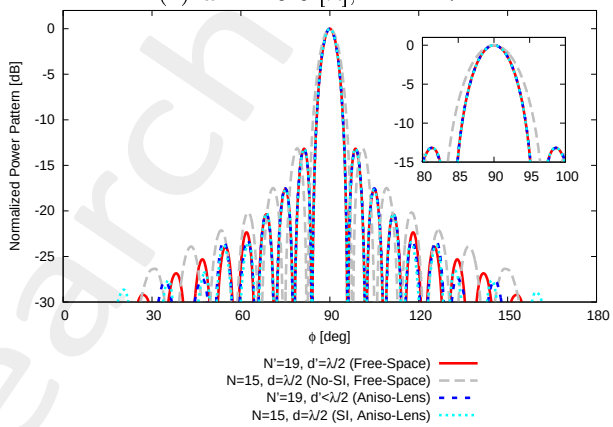

(d) $w' = 20.7$ $[\lambda]$, $N' = 19$

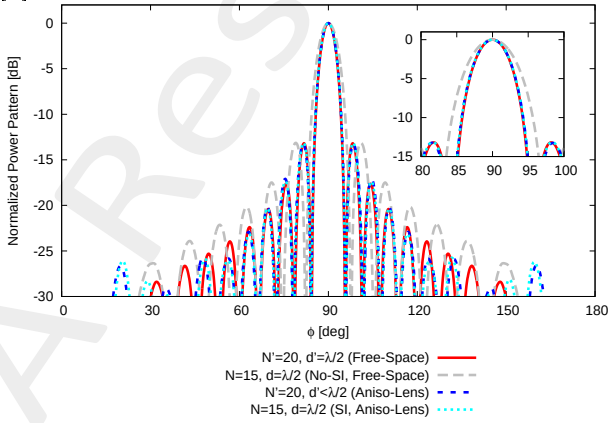

(e) $w' = 21.4$ $[\lambda]$, $N' = 20$

Figure 31: $\phi_s = 90$ [deg], $f = 600$ [MHz] - Far field pattern comparison for different values of w'.

1.3.3 Far-Field Patterns ($\phi_s = 75$ [deg], $f = 600$ [MHz])

Anisotropic Lens

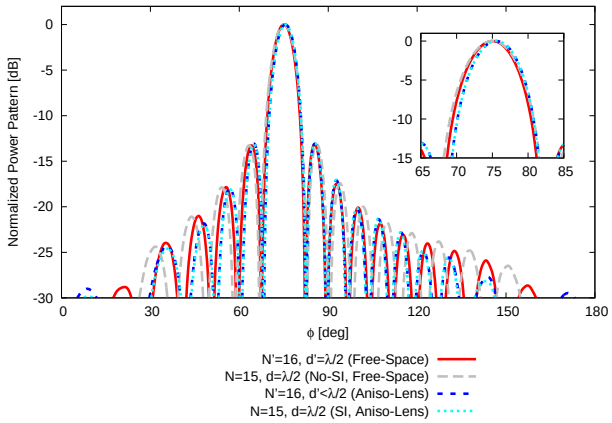

(a) $w' = 17.8$ [λ], $N' = 16$

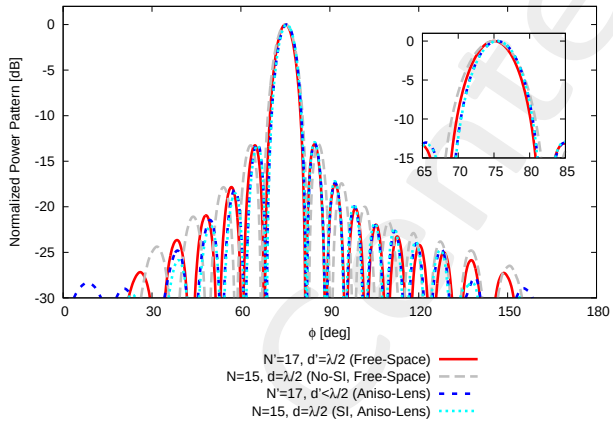

(b) $w' = 19.0$ [λ], $N' = 17$

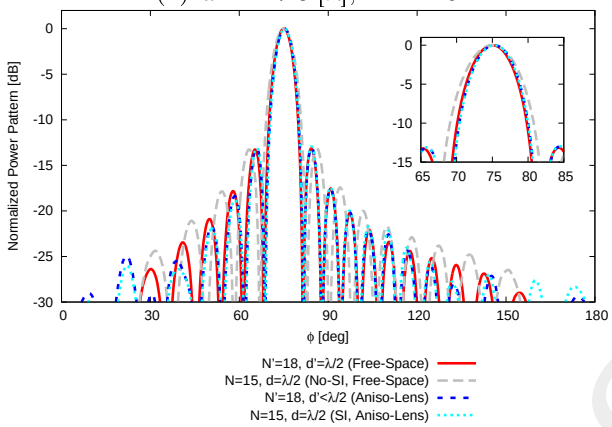

(c) $w' = 19.8$ [λ], $N' = 18$

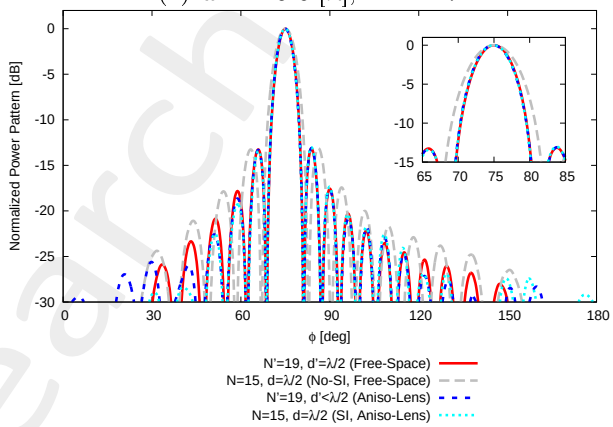

(d) $w' = 20.7$ [λ], $N' = 19$

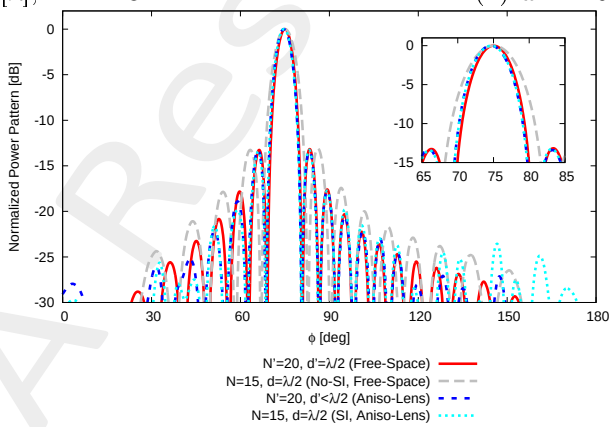

(e) $w' = 21.4$ [λ], $N' = 20$

Figure 32: $\phi_s = 75$ [deg], $f = 600$ [MHz] - Far field pattern comparison for different values of w'.

1.3.4 Far-Field Patterns ($\phi_s = 60$ [deg], $f = 600$ [MHz])

Anisotropic Lens

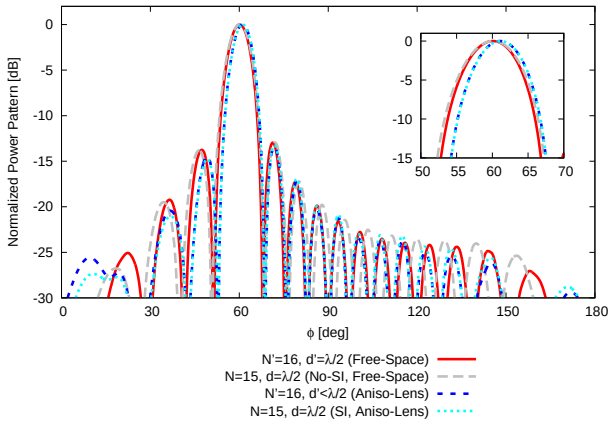

(a) $w' = 17.8$ $[\lambda]$, $N' = 16$

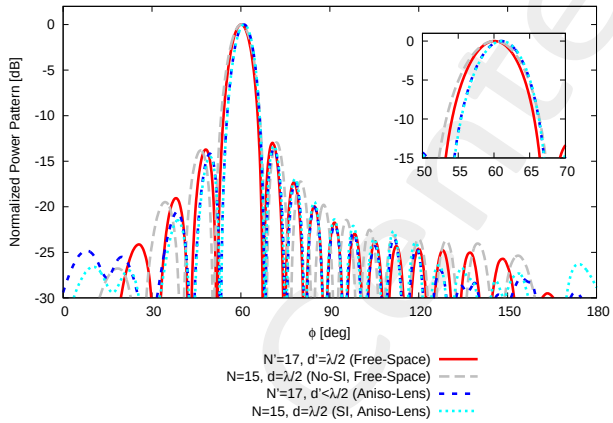

(b) $w' = 19.0$ $[\lambda]$, $N' = 17$

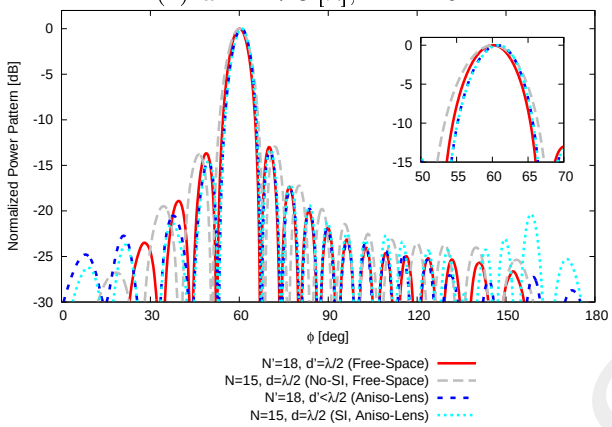

(c) $w' = 19.8$ $[\lambda]$, $N' = 18$

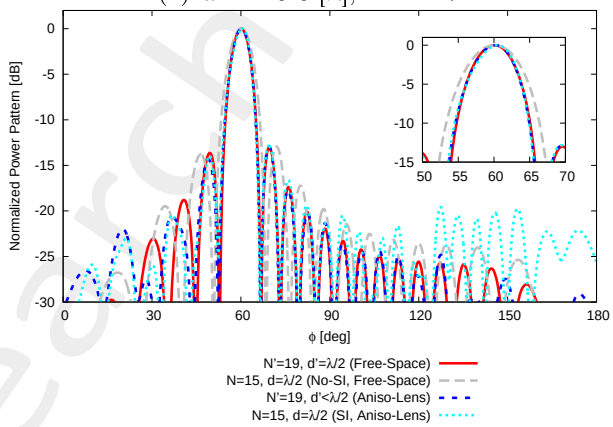

(d) $w' = 20.7$ $[\lambda]$, $N' = 19$

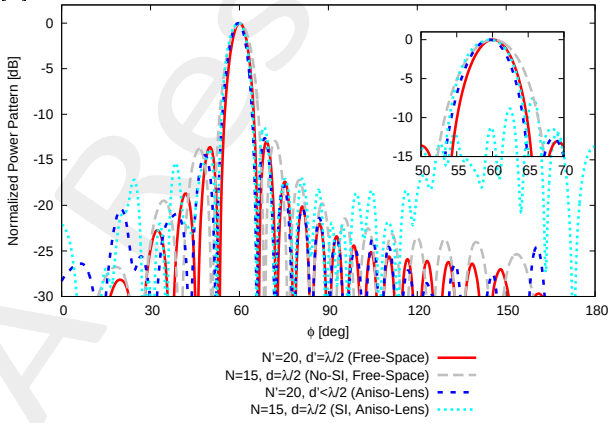

(e) $w' = 21.4$ $[\lambda]$, $N' = 20$

Figure 33: $\phi_s = 60$ [deg], $f = 600$ [MHz] - Far field pattern comparison for different values of w'.

1.3.5 Far-Field Patterns ($\phi_s = 95$ [deg], $f = 600$ [MHz])

Anisotropic Lens

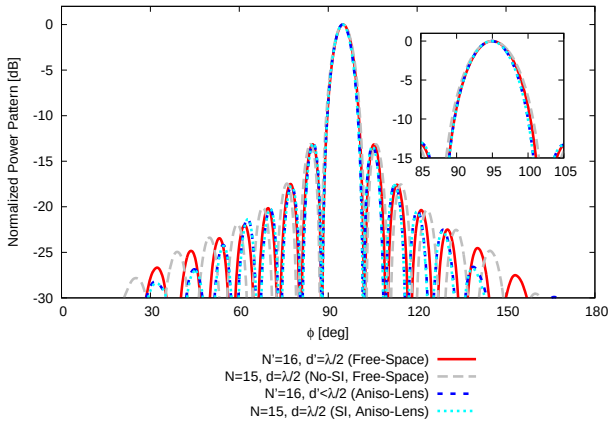

(a) $w' = 17.8$ [λ], $N' = 16$

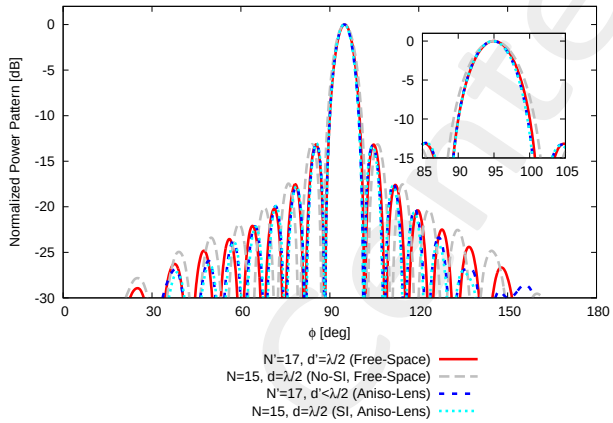

(b) $w' = 19.0$ [λ], $N' = 17$

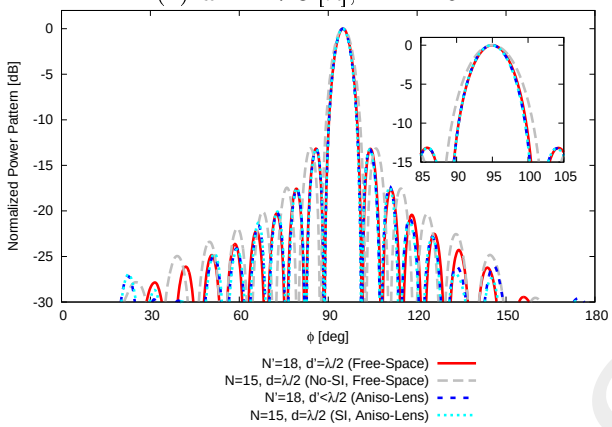

(c) $w' = 19.8$ [λ], $N' = 18$

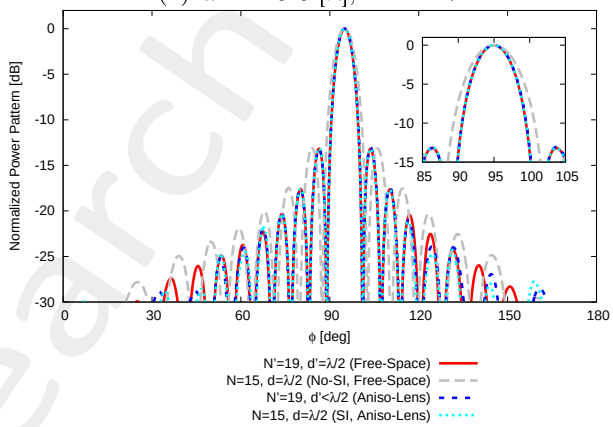

(d) $w' = 20.7$ [λ], $N' = 19$

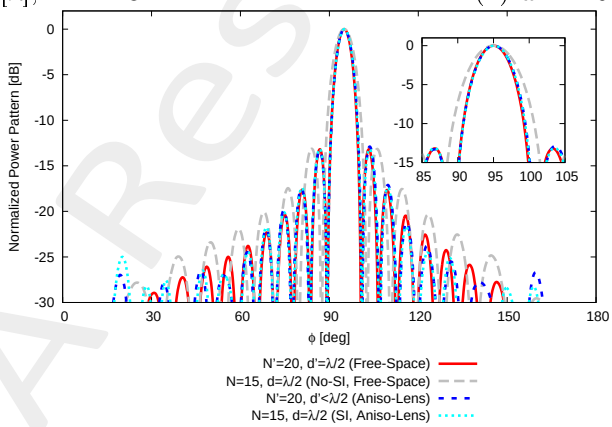

(e) $w' = 21.4$ [λ], $N' = 20$

Figure 34: $\phi_s = 95$ [deg], $f = 600$ [MHz] - Far field pattern comparison for different values of w'.

1.3.6 Far-Field Patterns ($\phi_s = 100$ [deg], $f = 600$ [MHz])

Anisotropic Lens

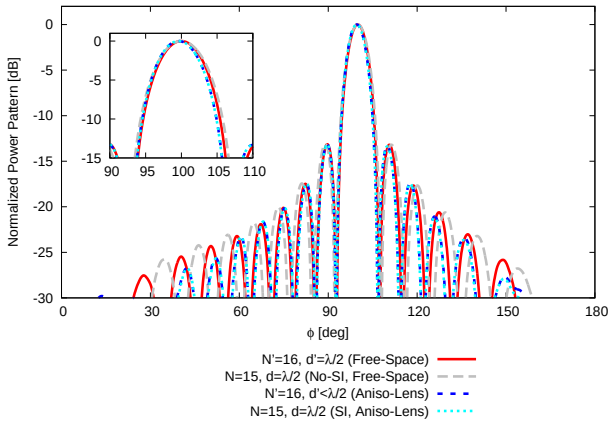

(a) $w' = 17.8$ $[\lambda]$, $N' = 16$

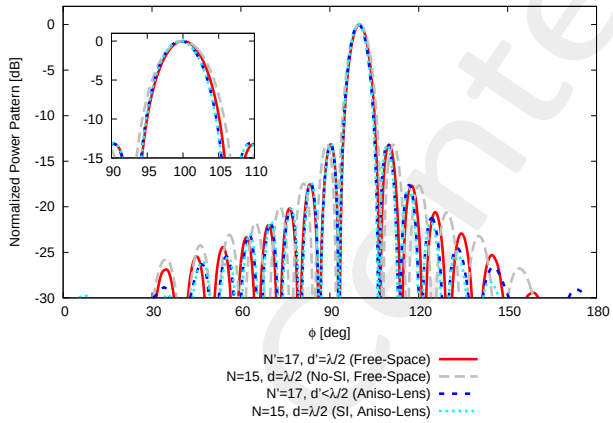

(b) $w' = 19.0$ $[\lambda]$, $N' = 17$

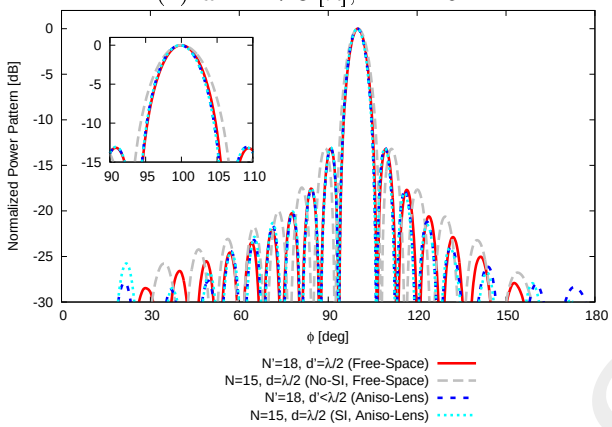

(c) $w' = 19.8$ $[\lambda]$, $N' = 18$

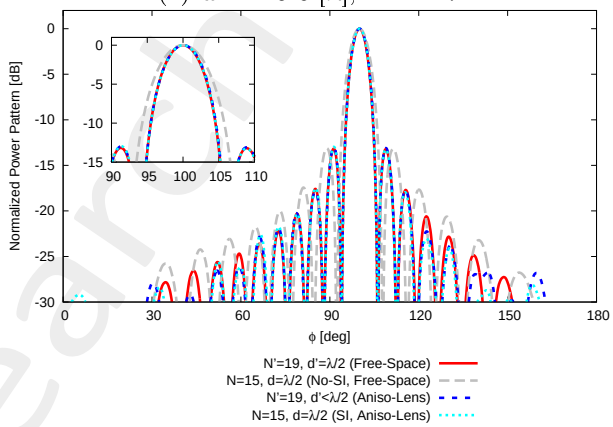

(d) $w' = 20.7$ $[\lambda]$, $N' = 19$

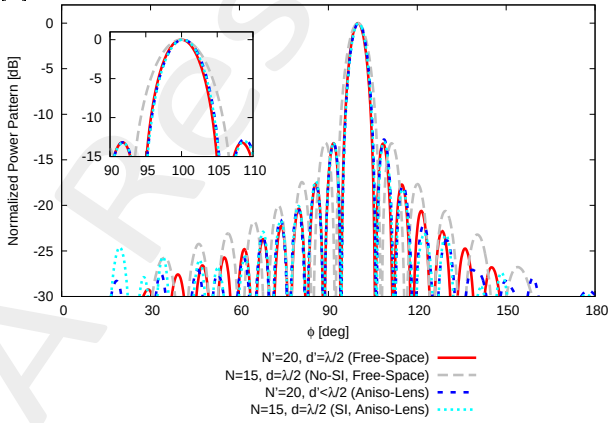

(e) $w' = 21.4$ $[\lambda]$, $N' = 20$

Figure 35: $\phi_s = 100$ [deg], $f = 600$ [MHz] - Far field pattern comparison for different values of w'.

1.3.7 Far-Field Patterns ($\phi_s = 105$ [deg], $f = 600$ [MHz])

Anisotropic Lens

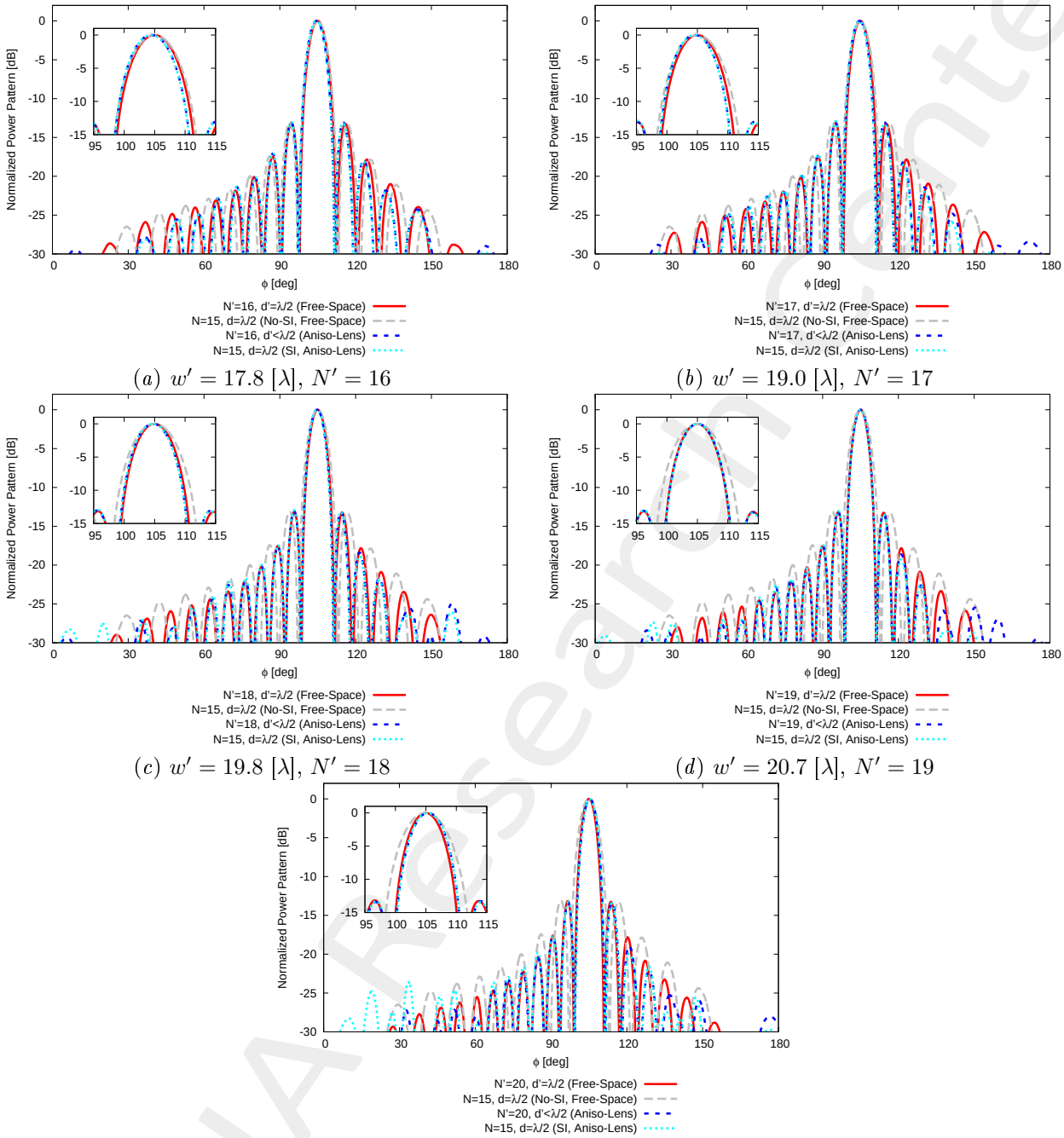

(a) $w' = 17.8$ $[\lambda]$, $N' = 16$

(b) $w' = 19.0$ $[\lambda]$, $N' = 17$

(c) $w' = 19.8$ $[\lambda]$, $N' = 18$

(d) $w' = 20.7$ $[\lambda]$, $N' = 19$

(e) $w' = 21.4$ $[\lambda]$, $N' = 20$

Figure 36: $\phi_s = 105$ [deg], $f = 600$ [MHz] - Far field pattern comparison for different values of w'.

1.3.8 Far-Field Patterns ($\phi_s = 110$ [deg], $f = 600$ [MHz])

Anisotropic Lens

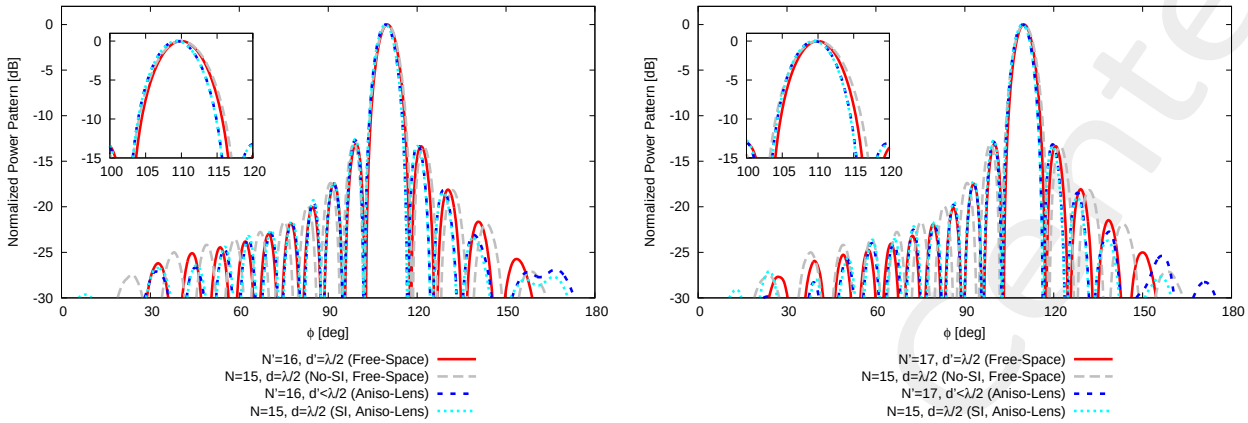

(a) $w' = 17.8$ $[\lambda]$, $N' = 16$

(b) $w' = 19.0$ $[\lambda]$, $N' = 17$

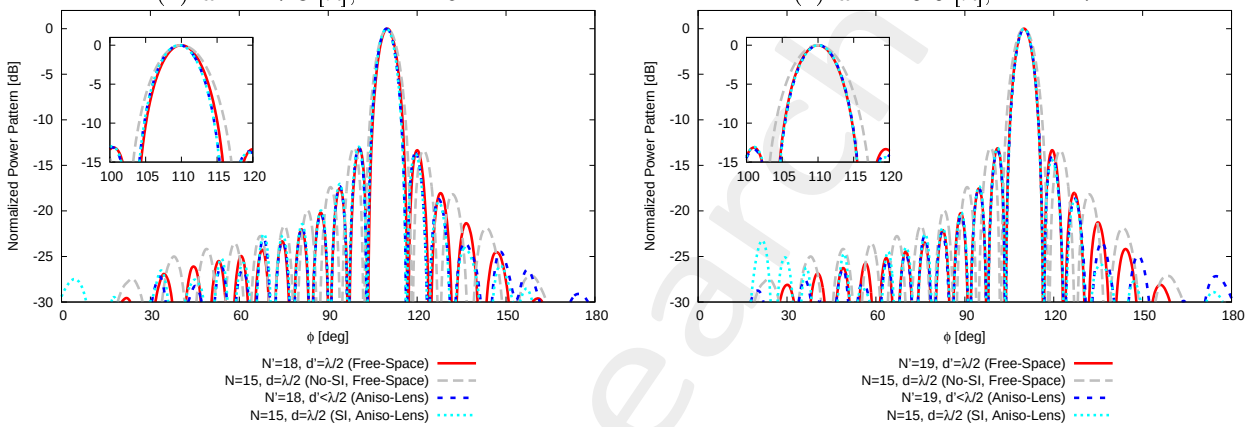

(c) $w' = 19.8$ $[\lambda]$, $N' = 18$

(d) $w' = 20.7$ $[\lambda]$, $N' = 19$

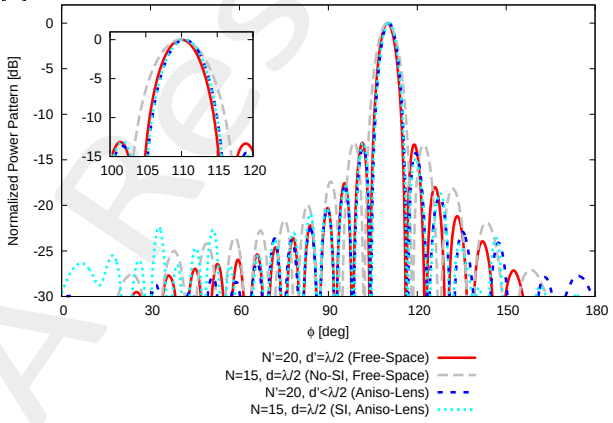

(e) $w' = 21.4$ $[\lambda]$, $N' = 20$

Figure 37: $\phi_s = 110$ [deg], $f = 600$ [MHz] - Far field pattern comparison for different values of w'.

1.3.9 Far-Field Patterns ($\phi_s = 120$ [deg], $f = 600$ [MHz])

Anisotropic Lens

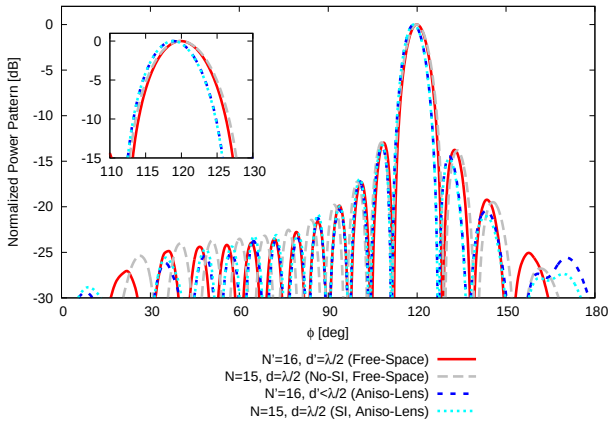

(a) $w' = 17.8$ $[\lambda]$, $N' = 16$

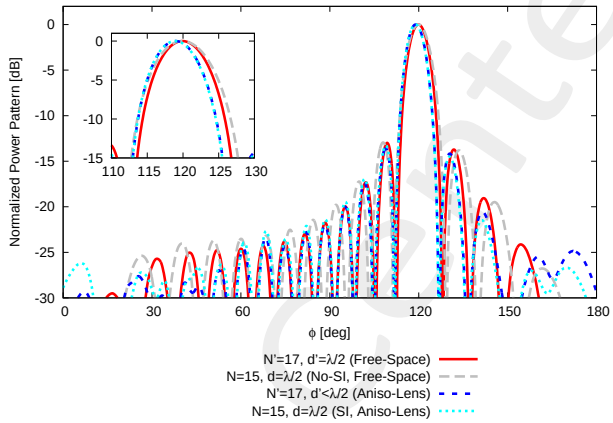

(b) $w' = 19.0$ $[\lambda]$, $N' = 17$

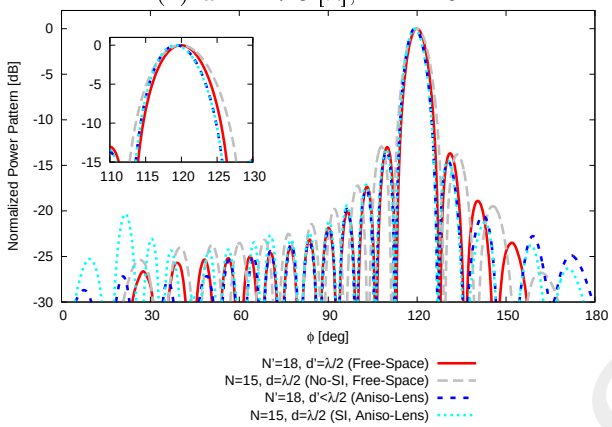

(c) $w' = 19.8$ $[\lambda]$, $N' = 18$

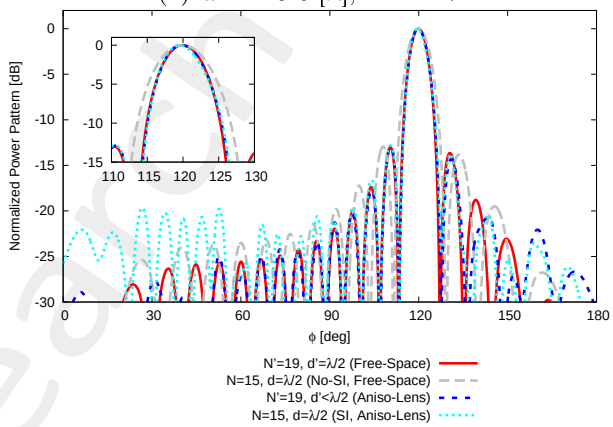

(d) $w' = 20.7$ $[\lambda]$, $N' = 19$

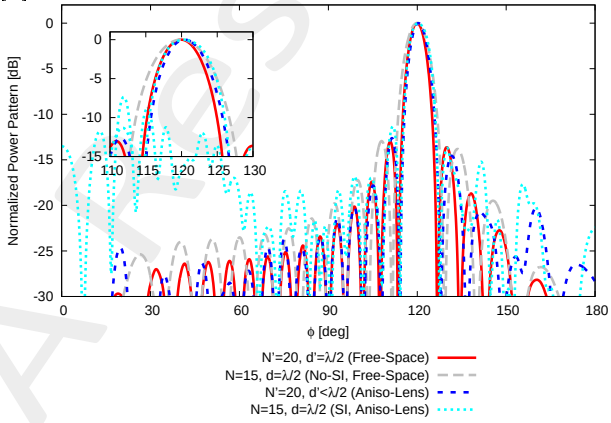

(e) $w' = 21.4$ $[\lambda]$, $N' = 20$

Figure 38: $\phi_s = 120$ [deg], $f = 600$ [MHz] - Far field pattern comparison for different values of w'.

1.4 Analysis vs. Frequency

Parameters

- Design frequency : $f_0 = 600$ [MHz] (central frequency);
- Relative bandwidth: $BW = \frac{f_{\max} - f_{\min}}{f_0} \times 100 = 25\%$;
- Minimum frequency: $f_{\min} = f_0 \times \left(1 - 0.5 \times \frac{BW}{100}\right) = 525$ [MHz];
- Maximum frequency: $f_{\max} = f_0 \times \left(1 + 0.5 \times \frac{BW}{100}\right) = 675$ [MHz];
- Number of frequency steps in $[f_{\min}, f_{\max}]$: $H = 5$.

1.4.1 Radiation pattern characteristics vs. frequency

Steering at $\phi_s = 90$ [deg]

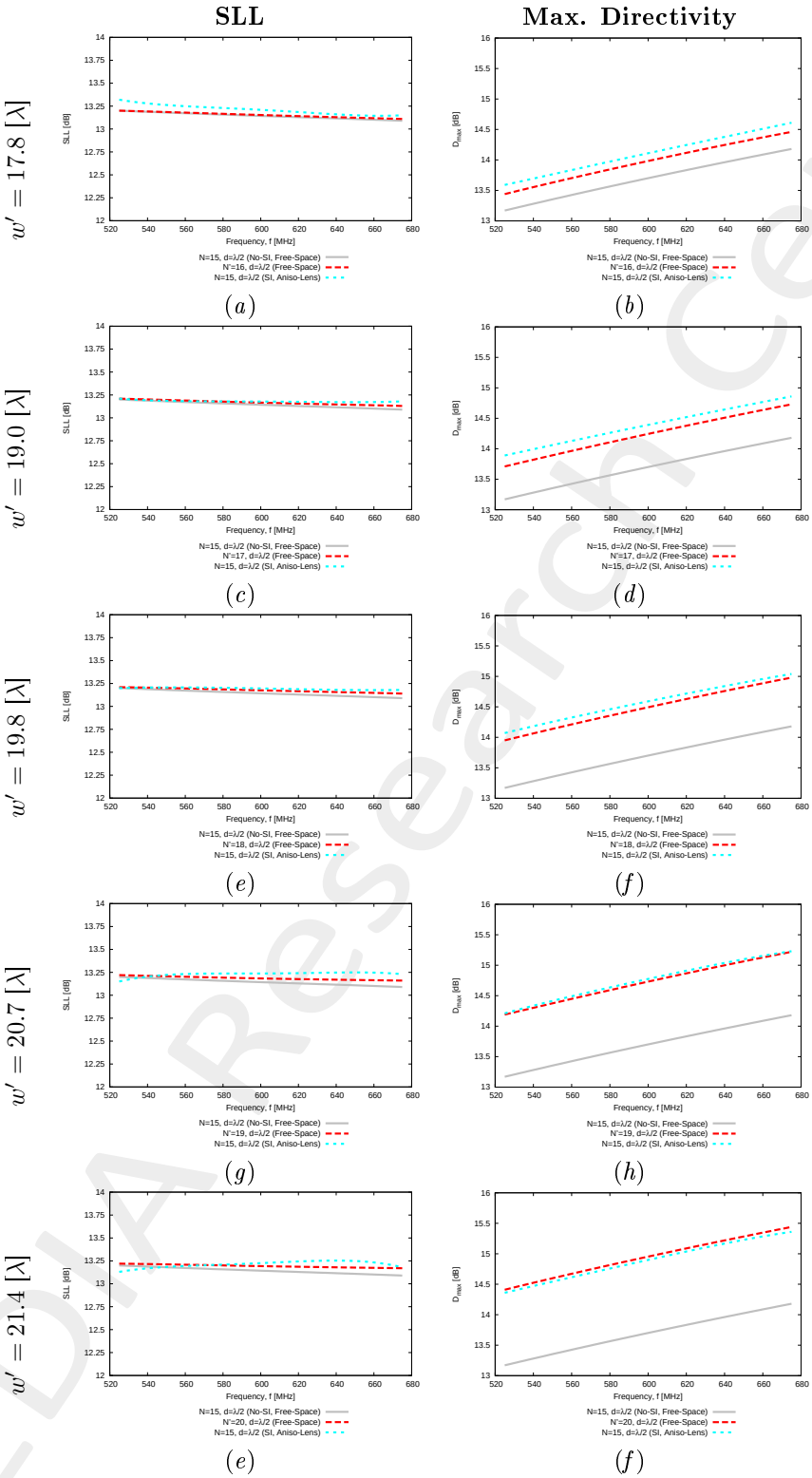

Figure 39: Aniso-Lens - Pattern performances (SLL and $D_{\max}$) vs. frequency.

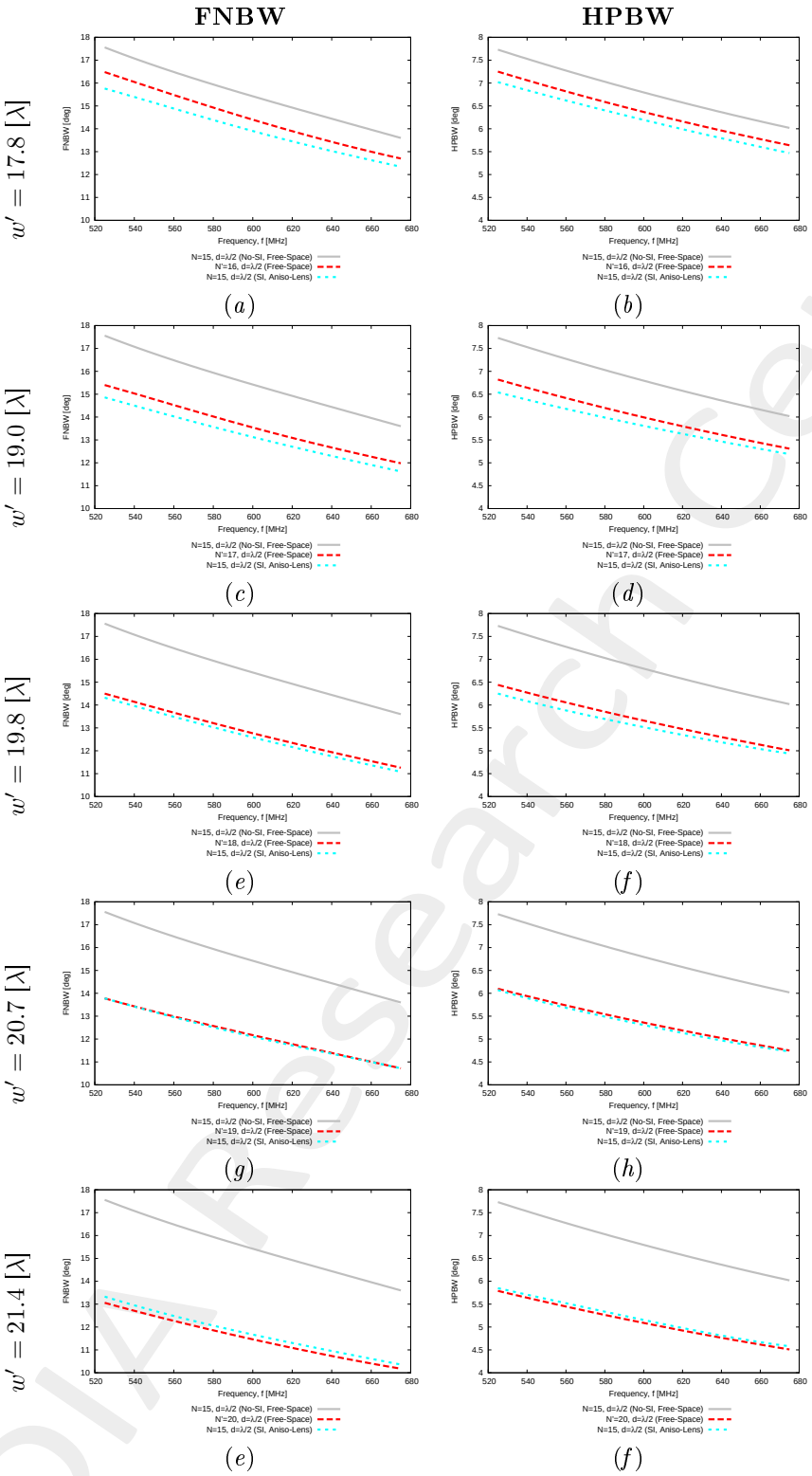

Figure 40: Aniso-Lens - Pattern performances ($FNBW$ and $HPBW$) vs. frequency.

References

[1] G. Oliveri, G. Gottardi, F. Robol, A. Polo, L. Poli, M. Salucci, M. Chuan, C. Massagrande, P. Vinetti, M. Mattivi, R. Lombardi, and A. Massa, "Co-design of unconventional array architectures and antenna elements for 5G base station," *IEEE Trans. Antennas Propag.*, vol. 65, no. 12, pp. 6752-6767, Dec. 2017.

[2] P. Rocca, G. Oliveri, R. J. Mailloux, and A. Massa, "Unconventional phased array architectures and design methodologies - A review," *Proc. IEEE*, vol. 104, no. 3, pp. 544-560, Mar. 2016.

[3] G. Oliveri, M. Salucci, N. Anselmi and A. Massa, "Multiscale System-by-Design synthesis of printed WAIMs for waveguide array enhancement," *IEEE J. Multiscale Multiphysics Computat. Techn.*, vol. 2, pp. 84-96, 2017.

[4] A. Massa and G. Oliveri, "Metamaterial-by-Design: Theory, methods, and applications to communications and sensing - Editorial," *EPJ Applied Metamaterials*, vol. 3, no. E1, pp. 1-3, 2016.

[5] L. Poli, G. Oliveri, P. Rocca, M. Salucci, and A. Massa, "Long-Distance WPT Unconventional Arrays Synthesis," *J. Electromagnet. Wave.*, vol. 31, no. 14, pp. 1399-1420, Jul. 2017.

[6] G. Oliveri, F. Viani, N. Anselmi, and A. Massa, "Synthesis of multi-layer WAIM coatings for planar phased arrays within the system-by-design framework," *IEEE Trans. Antennas Propag.*, vol. 63, no. 6, pp. 2482-2496, Jun. 2015.

[7] G. Oliveri, L. Tenuti, E. Bekele, M. Carlin, and A. Massa, "An SbD-QCTO approach to the synthesis of isotropic metamaterial lenses," *IEEE Antennas Wireless Propag. Lett.*, vol. 13, pp. 1783-1786, 2014.

[8] G. Oliveri, D. H. Werner, and A. Massa, "Reconfigurable electromagnetics through metamaterials - A review" *Proc. IEEE*, vol. 103, no. 7, pp. 1034-1056, Jul. 2015.

[9] G. Oliveri, E. T. Bekele, M. Salucci, and A. Massa, "Transformation electromagnetics miniaturization of sectoral and conical horn antennas," *IEEE Trans. Antennas Propag.*, vol. 64, no. 4, pp. 1508-1513, Apr. 2016.

[10] G. Oliveri, E. T. Bekele, M. Salucci, and A. Massa, "Array miniaturization through QCTO-SI metamaterial radomes," *IEEE Trans. Antennas Propag.*, vol. 63, no. 8, pp. 3465-3476, Aug. 2015.

[11] G. Oliveri, E. T. Bekele, D. H. Werner, J. P. Turpin, and A. Massa, "Generalized QCTO for metamaterial-lens-coated conformal arrays," *IEEE Trans. Antennas Propag.*, vol. 62, no. 8, pp 4089-4095, Aug. 2014.

[12] G. Oliveri, E. Bekele, M. Carlin, L. Tenuti, J. Turpin, D. H. Werner, and A. Massa, "Extended QCTO for innovative antenna system designs," IEEE Antenna Conference on Antenna Measurements and Applications (CAMA 2014), pp. 1-3, Nov. 16-19, 2014.

[13] G. Oliveri, P. Rocca, M. Salucci, E. T. Bekele, D. H. Werner, and A. Massa, "Design and synthesis of innovative metamaterial-enhanced arrays," IEEE International Symposium on Antennas Propag. (APS/URSI 2013), Orlando, Florida, USA, pp. 972 - 973, Jul. 7-12, 2013.

[14] G. Oliveri, "Improving the reliability of frequency domain simulators in the presence of homogeneous metamaterials - A preliminary numerical assessment," *Progress In Electromagnetics Research*, vol. 122, pp. 497-518, 2012.

[15] M. Salucci, G. Oliveri, N. Anselmi, G. Gottardi, and A. Massa, "Performance enhancement of linear active electronically-scanned arrays by means of MbD-synthesized metalenses," *J. Electromagnet. Wave.*, vol. 0, no. 0, pp. 1-29, 2017 (DOI: 10.1080/09205071.2017.1410077).